LITHOS 400–401 (2021) 106395

Contents lists available at ScienceDirect

LITHOS

journal homepage: www.elsevier.com/locate/lithos

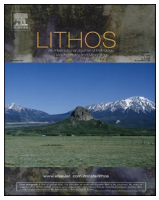

Research Article

Geochemistry and mineralogy of the Jebel Aja Igneous Intrusion and the associated exotic pegmatites, Arabian Shield, Saudi Arabia

Hisham A. Gahlan [a,b,*], Paul D. Asimow [c], Mokhles K. Azer [d], Chi Ma [c], Khaled M. Al-Kahtany [e], Alaa Y. Hakeem [a]

[a] Geology and Geophysics Department, College of Sciences, King Saud University, Riyadh 11451, Saudi Arabia
[b] Geology Department, Faculty of Science, Assiut University, Assiut 71516, Egypt
[c] Division of Geological & Planetary Sciences, California Institute of Technology, Pasadena, CA 91125, USA
[d] Geological Sciences Department, National Research Centre, 12622 Dokki, Cairo, Egypt
[e] Seismic Studies Center, College of Science, King Saud University, Riyadh 11451, Saudi Arabia

ARTICLE INFO

Keywords:
Arabian Shield
Aja igneous intrusion
Pegmatites
Pyroxmangite
Thortveitite
Thalénite-(Y)
Bustamite

ABSTRACT

We describe the Jebel Aja igneous intrusion (JAII), which sits at the farthest northeastern edge of the exposed Arabian Shield in Saudi Arabia. The JAII consists of late Neoproterozoic post-collisional A-type granites, and was emplaced during tectonic extension. It is a composite pluton consisting of a granitic core (monzogranite, syenogranite and alkali feldspar granite) surrounded by a later phase of alkaline and peralkaline granites. Pegmatites occur as pockets and dykes at the contact between the alkaline/peralkaline granites and syenogranite. The pegmatites have sharp contacts with their host granites and show variable colors (principally pink and white), grain sizes, textures, and mineral compositions. We report here that the white pegmatites host pockets with a unique mineralogy that includes the first observation of pyroxmangite, thortveitite and thalénite-(Y) in the whole Arabian Shield as well as a novel (Sc, Y, vacancy)-rich pyroxenoid and a vacancy-rich bustamite with excess octahedral Si. The pyroxmangite-dominated lithology also features accessory quartz, albite, spessartine, pyrochroite, muscovite, and fluorite. The presence of pyroxmangite rather than rhodonite, together with vacancy-rich and Si-excess pyroxenes, suggests an elevated pressure of emplacement. The granites of the JAII are highly evolved and have undergone extreme fractional crystallization of feldspars, leading to increases in the concentration of volatile and incompatible elements in the residual melt, which resulted eventually in injection of coeval pegmatites into the mostly solidified host granite. The syenogranite and alkaline/peralkaline granite of the JAII contain sodic amphibole and have geochemical characteristics common among within-plate rare-metal bearing A-type rocks. They have positive Nb-Ta anomalies that increase from syenogranite to alkaline/peralkaline granite. The pink pegmatite is highly mineralized and contains high concentrations of Nb (1540–1769 μg/g), Ta (103–136 μg/g), Y (1116–1616 μg/g), Zr (6362–9707 μg/g), Hf (215–264 μg/g), Th (278–384 μg/g), U (110–147 μg/g), and ∑REE (2334–3251 μg/g).

1. Introduction

The Arabian-Nubian Shield (ANS), an assembly of Neoproterozoic (850–590 Ma) crystalline rocks, represents one of the largest tracts of juvenile crust on Earth (Johnson, 2003; Meert, 2003; Stoeser and Frost, 2006). It constitutes the northern part of the East African Orogen (Stern, 1994) and was a contiguous mass until the opening of the Red Sea, which divided it into the Nubian Shield to the west and the Arabian Shield to the east. The ANS comprises a collage of ophiolite sequences and associated volcanic arcs, which amalgamated during the assembly of West and East Gondwana and were then intruded by a voluminous range of geochemically distinctive granitoids and mafic-ultramafic intrusions (e.g., Abdel-Karim, 1992, 1996; Ali et al., 2010; Azer et al., 2017; Genna et al., 2002; Stern, 1994; Stoeser and Frost, 2006).

The Arabian Shield hosts a number of discrete post-collisional A-type alkaline/peralkaline igneous complexes and pegmatites with significant enrichment of rare metals (e.g., Abdallah et al., 2020; Abuamarah, 2020; Elliott et al., 1999; Moghazi et al., 2011, 2015; Qadhi Talal, 2007).

* Corresponding author at: Geology and Geophysics Department, College of Sciences, King Saud University, Riyadh 11451, Saudi Arabia.
E-mail address: hjhlan@ksu.edu.sa (H.A. Gahlan).

https://doi.org/10.1016/j.lithos.2021.106395
Received 18 May 2021; Received in revised form 14 July 2021; Accepted 22 July 2021
Available online 26 July 2021

Among these, the Jebel Aja igneous intrusion (JAII), outcropping at the very northeastern limit of basement outcrop, is a well-exposed example. The main rock units of the JAII have been studied by several authors (Abdallah et al., 2020; Abuamarah, 2020; Ekren et al., 1987; Hereher and Abdullah, 2017; Qadhi Talal, 2007; Stuckless et al., 1984), but there are no published studies of the pegmatites. Hence the main focus of this work is to present the first report concerning the exotic pegmatites associated with the JAII.

A number of the minerals hosted in these pegmatites (pyroxmangite, thortveitite, thalénite-(Y)) are reported here for the first time in the whole ANS, and two exotic Sc-rich phases found in cleavage-plane fill in the pyroxmangite are entirely new. Pyroxmangite, thortveitite and thalénite-(Y) are rare silicate minerals. Pyroxmangite ($MnSiO_3$) is a Mn-rich end-member of the pyroxenoid group, with some economic importance because of its use in jewelry and ornamental objects. It was first described by Ford and Bradley (1913) and its crystal structure was determined by Liebau (1959). Pyroxmangite is very similar to its dimorph rhodonite; they may occur together as bladed intergrowths

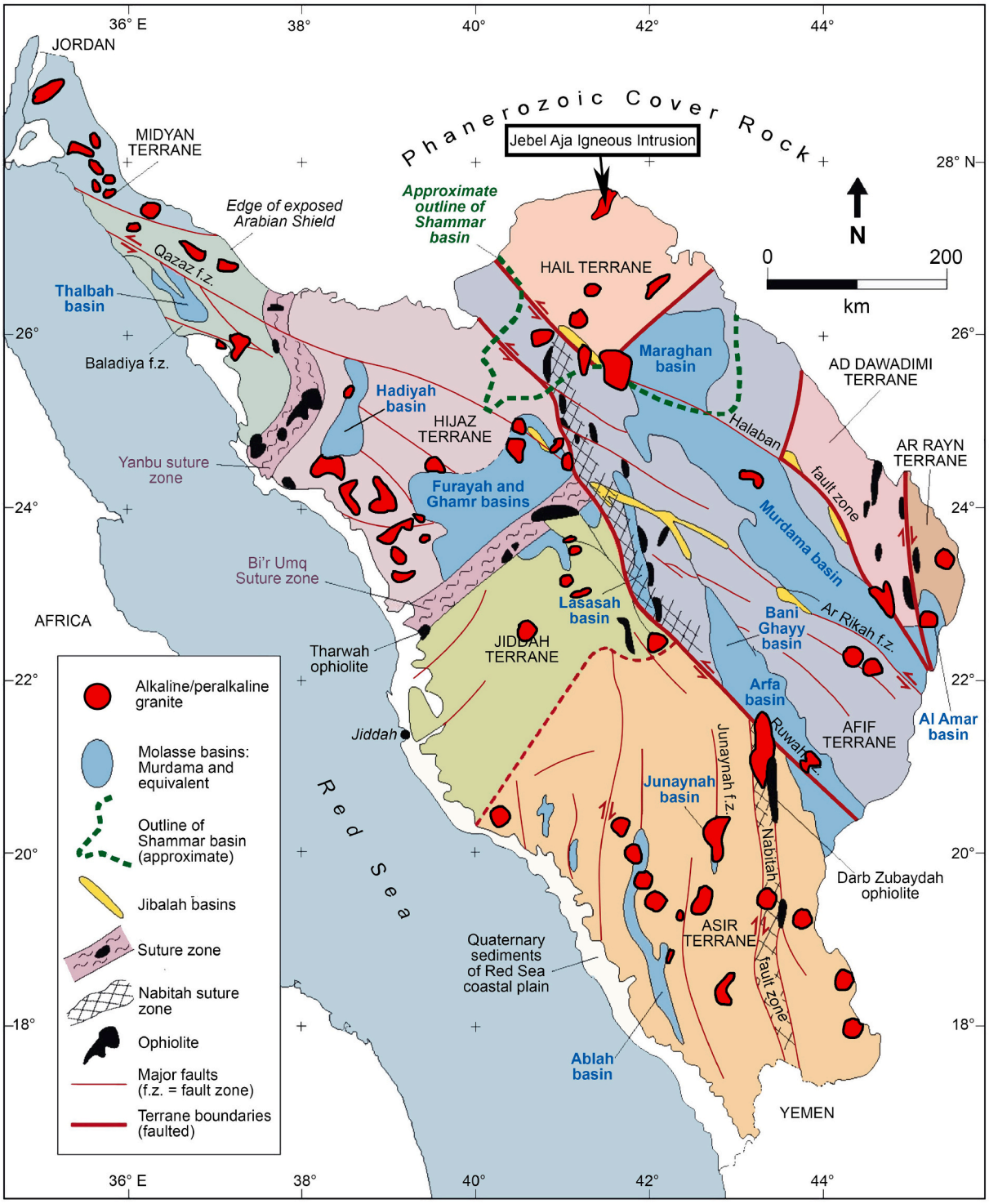

Fig. 1. Simplified geologic map of the Arabian Shield in Saudi Arabia (modified after Stern and Johnson, 2010), indicating the distribution of alkaline/peralkaline granites. The location of the Jebel Aja Igneous Intrusion is indicated.

(Jefferson et al., 1980; Michailidis and Sofianska, 2010; Millsteed et al., 2005; Ohashi et al., 1975; Pinckney and Burnham, 1988). Both are triclinic but they can be distinguished by Raman spectra or X-ray diffraction, and rhodonite generally contains higher Ca contents than pyroxmangite. The equilibrium phase boundary between pyroxmangite and rhodonite in pure $MnSiO_3$ has a positive Clapeyron slope, with pyroxmangite on the high-pressure, low-temperature side (Maresch and Mottana, 1976). Thortveitite is a scandium yttrium silicate mineral, nominally $(Sc,Y)_2Si_2O_7$. It is the primary source of scandium and occurs mainly in granitic pegmatites. Thalénite-(Y) has a nominal formula of $Y_3Si_3O_{10}F$, usually occurring within fluorite in granitic pegmatites.

The present study aims to provide complete mineralogical characterization of the JAII pegmatite mineralogy using classical methods and advanced techniques such as electron probe microanalyzer (EPMA), Raman spectroscopy, and scanning electron microscopy (SEM). This is presented alongside detailed geological, mineralogical, and geochemical context data on the host syenogranite and alkaline/peralkaline granite, in order to shed light on the magmatic sources and petrogenetic processes responsible for formation of the JAII and its pegmatites. We discuss the evidence for high pressure crystallization of the pegmatite mineralogy and its possible implications for vertical tectonic motions on the edge of the Arabian Shield in the post-collisional extensional period.

2. Geological setting

The Arabian Shield (Fig. 1) was formed by the accretion of intra-oceanic island arcs upon closure of the Mozambique Ocean (Nehlig et al., 2002; Robinson et al., 2014). It is characterized by presence of distinct terranes that are marked by the presence of ophiolitic ultramafic bodies within orogenic belts (Agar, 1992; Robinson et al., 2014). After the accretion, a period of extensional tectonism, orogenic collapse, and emplacement of post-collisional alkaline magmas resulted in one of the largest inventories of alkali granites in the world (Stoeser, 1986). Several of these A-type granites and associated pegmatites in the Arabian Shield are marked by significant enrichment of rare metals and rare earth elements (e.g., Abdallah et al., 2020; Abuamarah, 2020; Abuamarah et al., 2021; Drysdall et al., 1984; Drysdall and Douch, 1986; Elliott et al., 1999; Jackson and Douch, 1986; Johnson and Kattan, 2012; Küster, 2009; Moghazi et al., 2011).

The JAII is a Late Neoproterozoic Ediacaran intrusion of post-collisional A-type granitoids exposed along the northeastern edge of the Arabian Shield (Fig. 1). It is a generally elliptical body with irregular outlines, extended along a NE-SW axis (Fig. 2). At the outcrop boundaries, the JAII disappears under alluvial deposits that may cover a larger intrusion; original intrusive or tectonic contacts with country rocks are not exposed. The JAII is a composite igneous complex featuring two phases of magmatic activity, with sharp intrusive contacts between products of the two phases. The core of the intrusion includes a continuous sequence of monzogranite, syenogranite and alkali feldspar granite, with gradational contacts among the petrologic varieties. This phase contains numerous mafic microgranular enclaves (MMEs) and gneissic xenoliths. The core phase is entirely surrounded by alkaline to peralkaline granites and their volcanic equivalents, which we interpret as a later magmatic phase. Some roof pendants of the early granites are

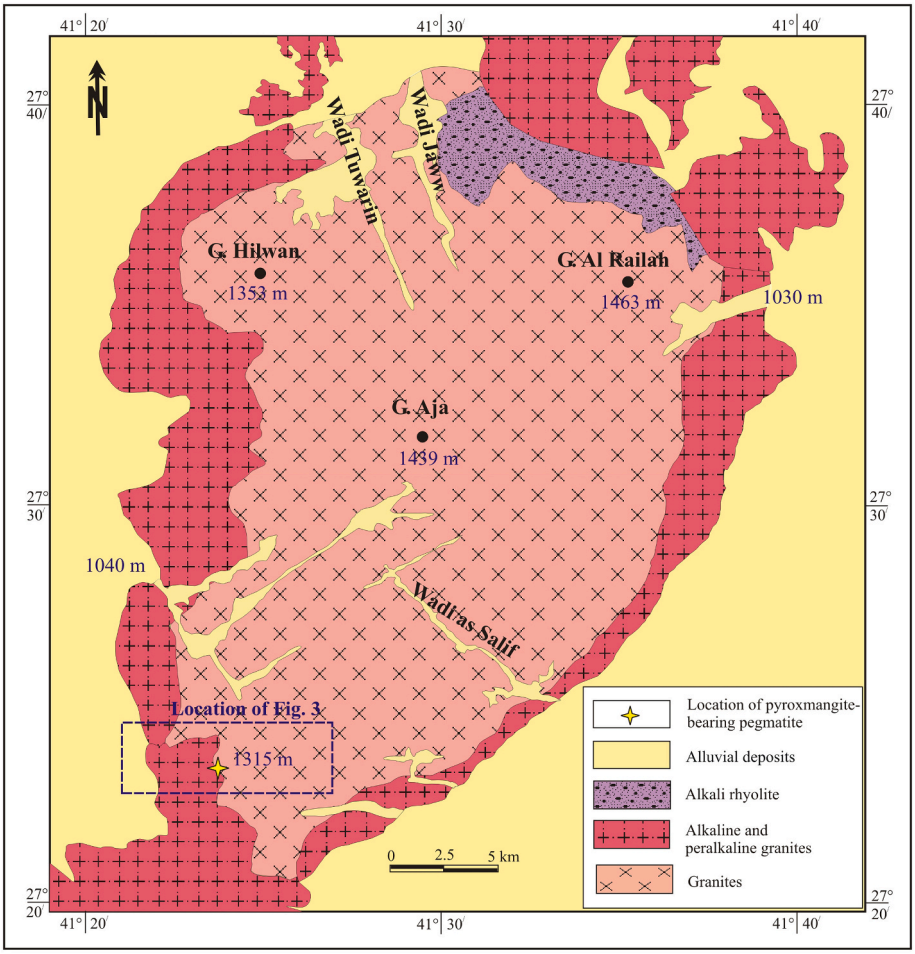

Fig. 2. Geological map of the Jebel Aja Igneous Intrusion, showing the major rock units (modified after Hereher and Abdullah, 2017). The location of Fig. 3 is indicated. The elevations of the major peaks and drainage points are given.

observed above the alkaline/peralkaline granites (Fig. 3).

The JAII is dissected by many dykes and later faults (not resolved at the scale of Fig. 2), especially the early phase. A stratified sequence of pyroclastic deposits, ignimbrites, and typical rhyolite flows unconformably overlies the early granitic phase and is intruded by alkaline/peralkaline granite. Pockets and dykes of pegmatite are found along the contact between the alkaline/peralkaline granites and syenogranite (Fig. 3a). The field relations of the JAII and its alluvial cover are summarized by a schematic cross-section in Fig. 3b, emphasizing the position of the pegmatites along the contact between the two phases of the intrusion.

The contacts between pegmatites and their host granites are almost sharp; no evidence of reaction between pegmatite and host is observed. The pegmatite bodies show variable colors, grain sizes, textures, and mineral compositions. They are distinguished into pink pegmatite (K-feldspar rich) and white pegmatite (albite rich). Pockets of pyroxmangite-rich pegmatite (10–20 cm) are found within the white variety for the first time. Pink pegmatite occurs as large masses (1–5 m) or as sheets (1–2 m width); it is very coarse-grained (Fig. 4a). The white pegmatite (Fig. 4b) is less common than pink pegmatite and occurs as pockets (0.5–1.0 m) or as small dykes (0.50–1.5 m width). The pyroxmangite-rich pockets (5–20 cm) are medium- to coarse-grained (Fig. 4c).

3. Analytical methods

Whole rock geochemical analyses were performed at ALS Geochemistry, Vancouver BC, Canada. Whole rock samples were crushed and pulverized in an agate ring mill. Major elements were determined by Inductively Coupled Plasma-Atomic Emission

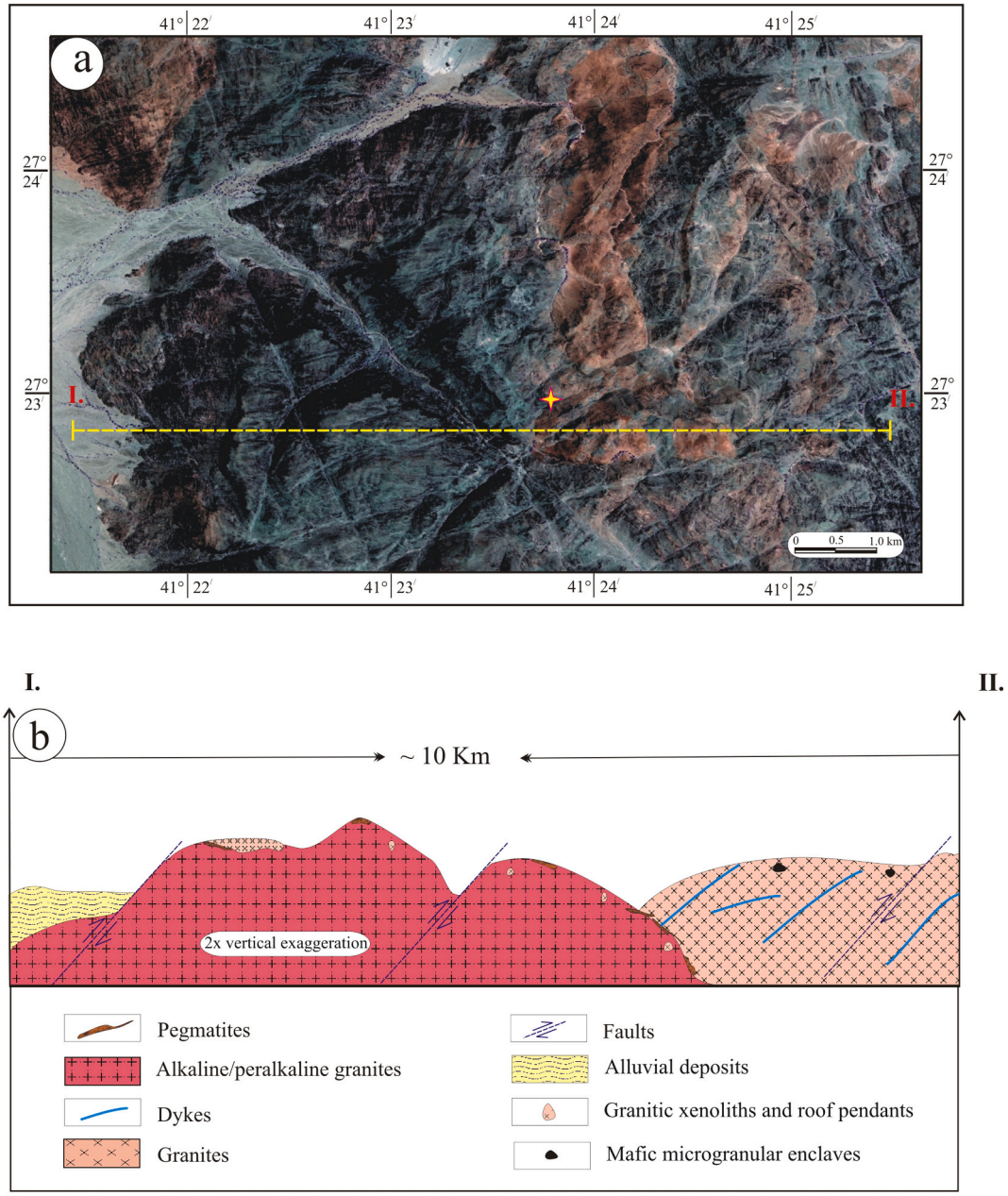

Fig. 3. (a) Aerial photo of a section of the Jebel Aja Igneous Intrusion showing the location of pegmatite bodies. (b) Schematic cross-section (2× vertical exaggeration) showing the field relationships between the pegmatites and the different rock types of the Jebel Aja Igneous Intrusion. Note line of section marked on Fig. 3a.

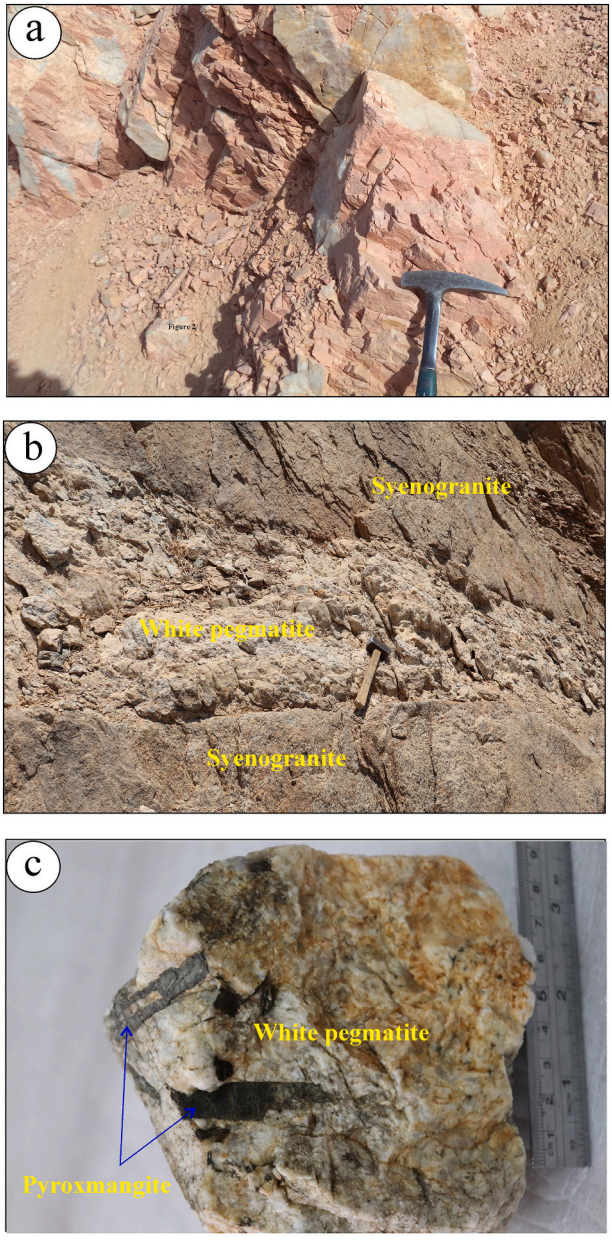

Fig. 4. Field photographs showing (a) outcrop of pink pegmatite, (b) white pegmatite body cutting syenogranite, and (c) pyroxmangite-bearing white pegmatite hand specimen. (For interpretation of the references to color in this figure legend, the reader is referred to the web version of this article.)

Spectroscopy (ICP-AES) following lithium metaborate/lithium tetraborate ($LiBO_2/Li_2B_4O_7$) fusion and digestion in 4% HNO_3/2% HCl. Trace elements, including rare earth elements, were determined by Inductively Coupled Plasma–Mass Spectrometry (ICP-MS) using the same digested solutions. Loss on ignition was determined by difference in weight after a 1 g sample was heated at 1000 °C for 1 h.

Chemical compositions of essential minerals in the pyroxmangite-bearing pegmatite, syenogranite, and peralkaline granites were carried out by electron probe microanalysis (EPMA) at Caltech (JEOL JXA-8200) on carbon-coated polished thin sections. Operating conditions were 15 kV accelerating voltage, 25 nA beam current, a focused beam (1 μm), 20 s on-peak counting times, the mean atomic number background subtraction method, a mix of natural and synthetic mineral standards, and the CITZAF matrix correction routine.

Backscattered electron images, energy dispersive X-ray spectra (EDS), and electron backscatter diffraction (EBSD) patterns were obtained with the Zeiss 1550VP field-emission scanning electron microscope (SEM) in the Division of Geological and Planetary Sciences at Caltech. To detect heavy elements, a 25 kV primary beam was chosen and spectra were collected either in the 0–10 kV or 0–20 kV range. Deadtime was maintained below 60% and spectra were integrated for 60 s of live time. The EDS detector is a Si-drift type Oxford Max and data were processed with Oxford's AZTec software, using factory standards for quantification. EBSD analyses were carried out using an HKL EBSD system on the ZEISS SEM, operated at 20 kV and 6 nA in focused-beam mode with a 70° tilted stage and variable pressure mode (25 Pa). EBSD patterns were also processed with AZTec, with structures matched to the American Mineralogist Crystal Structure Database and ICSD libraries.

Selected mineral identifications were further verified using Raman spectroscopy (Renishaw InVia micro-Raman spectrometer with 514 nm Ar-ion laser) at the GPS Division, California Institute of Technology (Caltech), USA. Spectra were collected at Raman shifts from 100 to 4000 cm^{-1} and spectra were compared to the RRUFF.info library for mineral identification.

4. Petrography

The granitic rocks of the JAII show wide variations in their textures and mineralogical compositions (Abdallah et al., 2020; Abuamarah, 2020). According to Abuamarah (2020), the early phase of the JAII includes monzogranite, syenogranite, granophyre and alkali feldspar granite, whereas the later phase includes alkaline granite and peralkaline granite. In the present work, the pegmatites associated with JAII are described for the first time. Brief petrographic descriptions of the pegmatites and their surrounding granites (syenogranite and alkaline/peralkaline granites) are given below.

4.1. Syenogranite

Syenogranite is inequigranular, medium- to coarse-grained, and pink to pale pink in color. It consists essentially of K-feldspar and quartz, with minor plagioclase and mafic minerals. Accessory minerals include Fe-Ti oxides, zircon, titanite and apatite. K-feldspar occurs as large anhedral crystals of orthoclase that contain small inclusions of albite and muscovite. The orthoclase crystals show perthitic texture with flame, patchy and veined types. Quartz occurs as anhedral to subhedral large crystals and small anhedral aggregates occupying the interstitial spaces between the feldspars. Locally, it forms graphic and myrmekitic intergrowths with K-feldspar. Plagioclase occurs as euhedral to subhedral tabular crystals of albite, which are usually corroded by quartz and K-feldspar, and as inclusions in K-feldspar. The mafic minerals are dominantly strongly pleochroic, subhedral to euhedral crystals of katophorite amphibole (Fig. 5a) with goethite inclusions. Aegirine is also present, as subhedral to anhedral prismatic crystals replaced along margins and cracks by goethite (Fig. 5b, c). Zircon occurs as interstitial fine crystals among the other constituents (Fig. 5b) or as inclusions in K-feldspar and amphibole.

4.2. Alkaline/peralkaline granites

The alkaline and peralkaline granites are similar in appearance and mineralogy. They are medium- to coarse-grained with a hypidiomorphic inequigranular texture and pink to pale pink color. Alkali feldspars and quartz are the main constituents, with mafic mineral in variable amounts. The alkaline/peralkaline granites feature a large variety of accessory minerals including zircon, fluorite, Fe-Ti oxides, xenotime, monazite, titanite, allanite, thorite and pyrochlore. The most prominent petrographic difference between the relative alkaline and peralkaline granite is the greater modal abundance of K-feldspar, sodic amphibole, and sodic pyroxene in the peralkaline type.

Perthitic alkali feldspar, unmixed into orthoclase and albite lamellae,

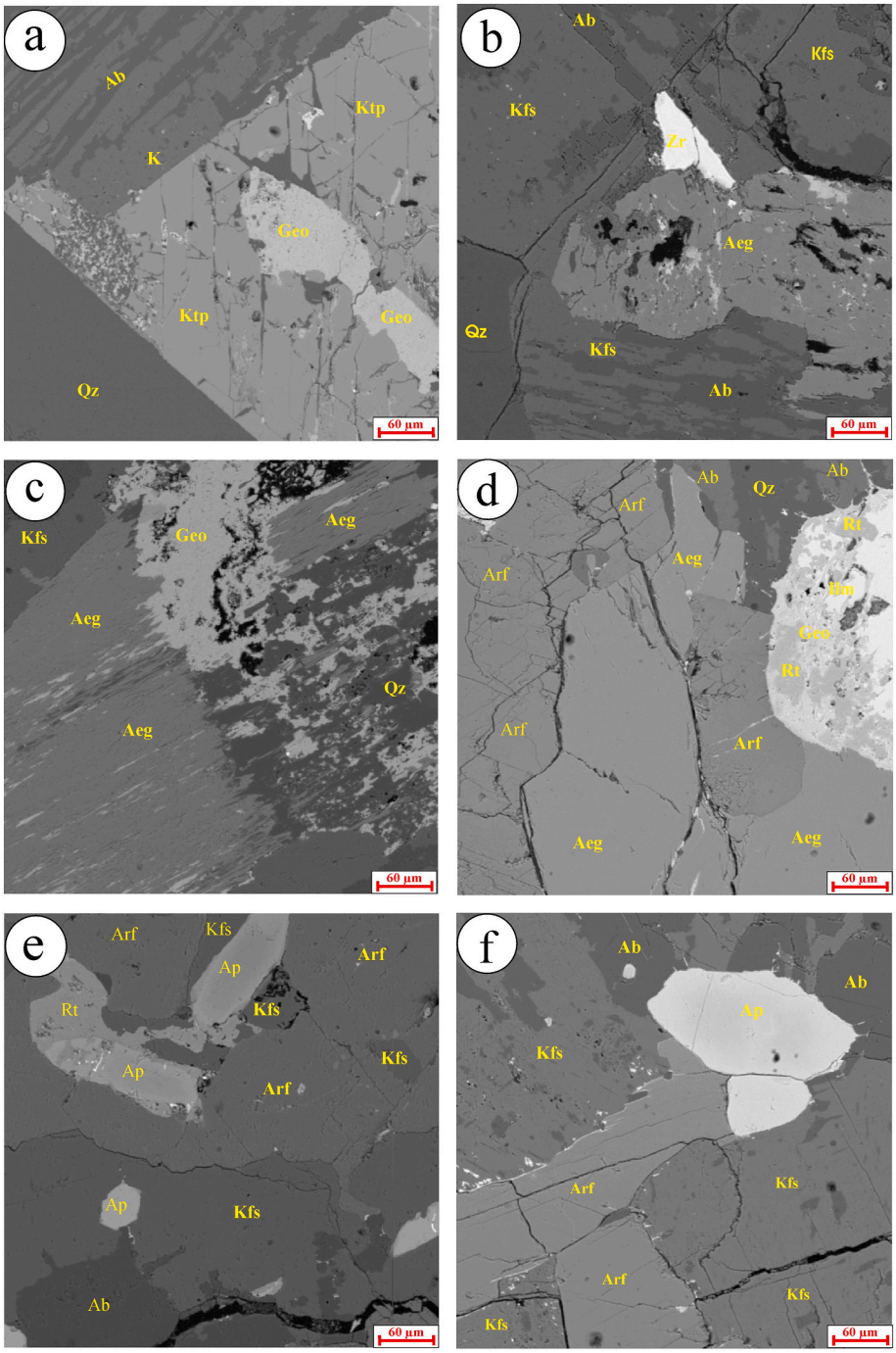

Fig. 5. Back-scattered electron images showing petrographic textures in the syenogranite and peralkaline granite: (a) crystals of katophorite in syenogranite, (b) interstitial crystals of aegirine and zircon in syenogranite, (c) aegirine crystals partly altered to goethite in syenogranite, (d) arfvedsonite and aegirine crystals in the peralkaline granite, (e) apatite inclusions in arfvedsonite and K-feldspar in the peralkaline granite, (f) interstitial apatite among arfvedsonite, albite and K-feldspar in the peralkaline granite. Mineral abbreviations: Qz = quartz, Ab = albite. Aeg = Aegirine, Kfs = K-feldspars, Arf = Arfvedsonite, Rt = Rutile, Ktp = katophorite, Zr = zircon, Ilm = Ilmenite, Ap = apatite, Goe = goethite.

is the dominant feldspar in both rock types, with smaller amounts of microcline. Perthitic textures include veined, flame, and patchy varieties. Some perthitic orthoclase crystals feature small inclusions of quartz and rare albite with forms that suggest inclusion rather than exsolution. No separate plagioclase crystals are present other than those forming the perthite or included in perthitic orthoclase. Quartz is not uniform in amount or distribution and occurs as aggregates of anhedral crystals or as small, rounded inclusions in perthitic orthoclase.

The alkaline mafic minerals include sodic amphibole and sodic pyroxene. The sodic amphibole is strongly pleochroic and occurs as anhedral to subhedral crystals or as interstitial acicular crystals. It ranges in composition from magnesio-arfvedsonite to arfvedsonite (Fig. 5d, e, f). Rare inclusions of zircon, Fe-Ti oxides and apatite are observed within sodic amphibole. Locally, sodic amphibole is transformed along its margins into opaques. Sodic pyroxene occurs as anhedral to subhedral crystals of aegirine associated with arfvedsonite (Fig. 5d).

Fluorite is the most abundant accessory mineral and occurs as anhedral interstitial crystals or as vein filling along fractures. These features indicate that the fluorite is a late-stage magmatic mineral. Fe-Ti oxides occur either as individual crystals or as granular aggregates associated with altered mafic minerals. They include rutile, goethite, ilmenite, and magnetite. Fine subhedral apatite crystals are found interstitially among the feldspars and sodic amphibole (Fig. 5e, f) or as inclusions in K-feldspar (Fig. 5e). Zircon occurs as separate interstitial crystals among the feldspars or as inclusions in the mafic minerals. Allanite occurs as euhedral crystals showing strong pleochroism from red to reddish-brown. Monazite occurs as euhedral to subhedral crystals

which associates with iron oxides. Titanite is common as euhedral rhombic crystals or as irregularly-shaped crystals associated with opaques. Thorite occurs as anhedral crystals with brownish-yellow, brownish-black, yellow and orange colors. A few thorite crystals are associated with xenotime.

4.3. Pegmatites

As noted above, pegmatites are distinguished into pink and white varieties with pyroxmangite-rich pockets in the white type.

Pink pegmatite is pink to reddish gray in color and very coarse-grained. It consists mainly of microcline, orthoclase (with perthitic lamellae of albite), and muscovite with minor albite and biotite. Iron oxides, zircon, fluorite and apatite are accessories. Small crystals of albite, iron oxides, and zircon are enclosed within orthoclase. Quartz shows undulose extinction and rarely contains fine inclusions of K-feldspar, albite and muscovite. A narrow zone of fine-grained recrystallized quartz and feldspar forms a mortar structure around the large feldspar grains.

White pegmatite is medium- to coarse-grained and consists of albite, quartz, K-feldspar, biotite, and muscovite. Opaques, allanite and zircon are accessory minerals. Albite occurs as euhedral to anhedral prismatic crystals characterized by lamellar twinning. It is intergrown with quartz forming graphic texture. Some albite cores are highly altered to sericite and muscovite; others are kaolinitized. K-feldspar occurs as subhedral crystals showing perthitic exsolutions of albite or as microcline showing cross-hatch twinning. Quartz appears in graphic intergrowths with albite, in small inclusions in albite and muscovite, in veinlets, and

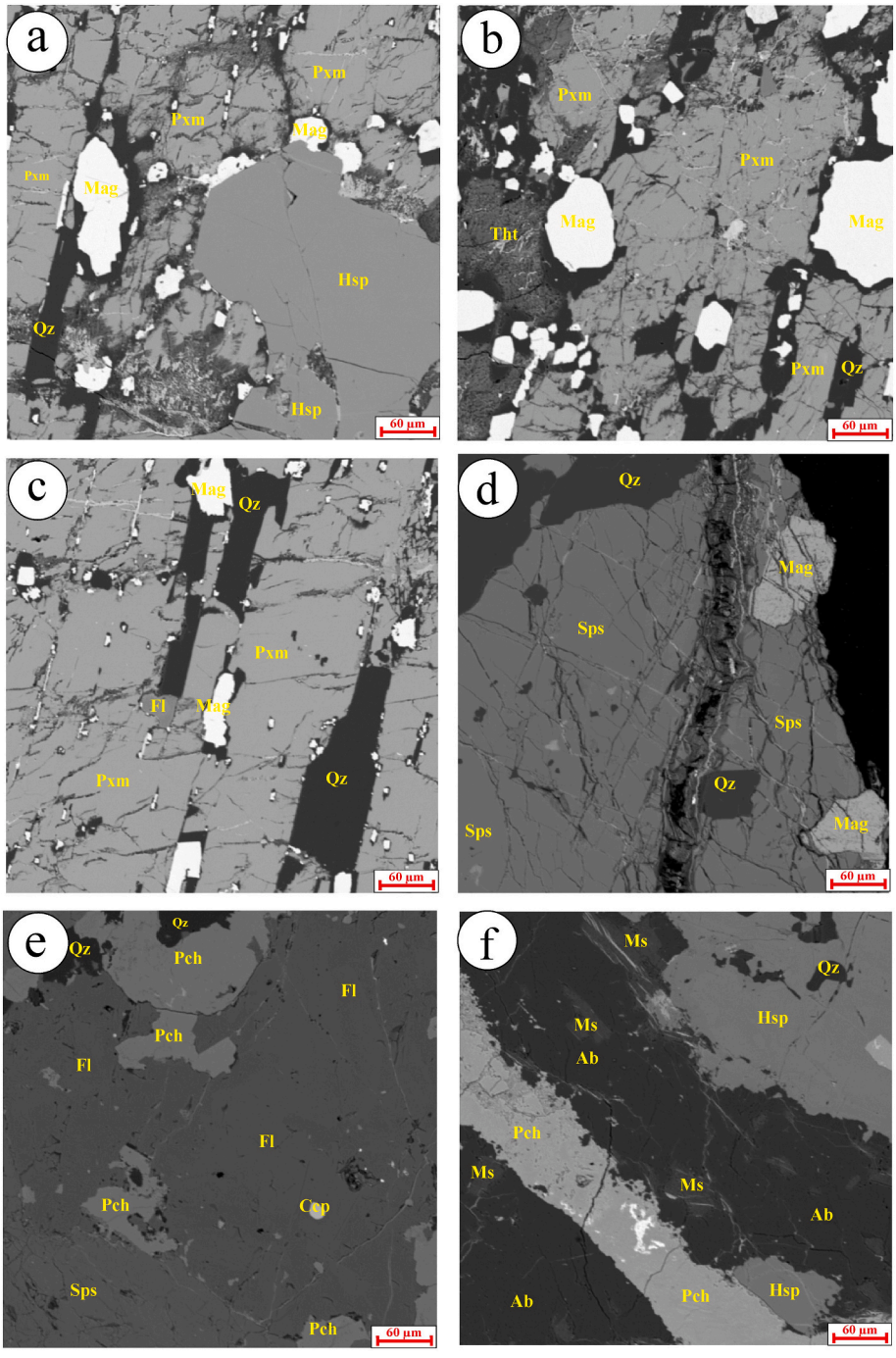

Fig. 6. Back-scattered electron images showing petrographic textures in the pyroxmangite-bearing white pegmatite sample: (a) Hydrospessartine, magnetite, and quartz included within large pyroxmangite crystal, (b) small crystal of thortveitite with magnetite and quartz included in large pyroxmangite crystal, (c) quartz-magnetite veinlets filling the cleavage planes in pyroxmangite, (d) crack in spessartine crystal filled with secondary minerals, (e) pyrochroite occurs as anhedral patches within the large fluorite crystal, (f) veinlets of pyrochroite and inclusions of muscovite in albite. Mineral abbreviations: Pxm = pyroxmangite, Qz = quartz, Mag = magnetite, Sps = spessartine, Hsp = hydrospessartine, Fl = fluorite, Ccp = chalocopyrite, Pch = pyrochroite, Ms. = muscovite, Ab = albite, Tht = Thortveitite.

distributed along grain boundaries between other minerals. Biotite occurs as fine anherdal crystals, altered along margins into chlorite. Muscovite is found as small flakes, interstitial or included in K-feldspar.

The pyroxmangite-rich pegmatite that is found in the JAII is the first record of this mineral in the Neoproterozoic rocks of the ANS. These pegmatite pockets are dominated by albite, pyroxmangite and spessartine with minor amounts of magnetite, muscovite and fluorite. The accessory minerals include pyrochroite (Mn hydroxide), thortveitite, thalénite-(Y), a Sc- and vacancy-rich pyroxmangite, and a Sc-bearing bustamite with excess Si. Pyroxmangite occurs as large (0.5–2 mm) anhedral crystals (Fig. 6a, b) and as fine as (~10 μm) needle-like crystals. The large pyroxmangite crystals are parted along perpendicular cleavage planes that are filled by quartz-magnetite veins (Fig. 6c). Garnet occurs as anhedral crystals of spessartine and hydrospessartine (Fig. 6a, d); the spessartine crystals are dissected by cracks filled with secondary minerals (Fig. 6d). Magnetite occurs as anhedral crystals within cleavage-plane veins in pyroxmangite (Fig. 6a, b, c). Fluorite occurs as large crystals containing pyrochroite inclusions (Fig. 6e). Pyrochroite occurs as anhedral patches within the large fluorite crystals (Fig. 6e) or filling veinlets (Fig. 6f). Muscovite occurs as fine anhedral crystals and as inclusions in the albite (Fig. 6f). A few crystals of thortveitite are found in the quartz- and magnetite-dominated veins filling cleavage planes in pyroxmangite (Fig. 6b). This is the first report of thortveitite in the ANS; it was identified on the basis of composition in EDS spectra and confirmed by EBSD, Raman and EPMA analyses. EDS and EPMA analysis also identified numerous laths of two novel pyroxene-related phases, further characterized below.

5. Electron microprobe, SEM/EDS, EBSD and Raman spectroscopy analyses

The identification of the minerals under the microscope was refined and supported by EPMA, SEM/EDS, EBSD and Raman methods. EPMA analyses of the essential minerals were performed in samples of syenogranite, peralkaline granite, and pyroxmangite-bearing pegmatite. The analyzed minerals in the syenogranite and peralkaline granite included K-feldspar, albite, katophorite, sodic amphibole, aegirine, Fe-Ti oxides and apatite. The analyzed minerals in the pyroxmangite-rich pegmatite sample are pyroxmangite, garnet, pyrochroite, muscovite, albite, magnetite, fluorite, thortveitite, thalénite-(Y), and the two Sc-rich pyroxene-related phases. Where compositional analysis is insufficient to uniquely identify mineral species, Raman spectroscopy and EBSD helped confirm the inferences from petrography and microprobe analyses. The entire microprobe data are presented, divided by mineral species, in supplementary tables (1S–15S).

5.1. Amphiboles

Amphiboles were analyzed in syenogranite and peralkaline granite; their chemical compositions and structural formulae are listed in Supplementary Table 1S. Amphibole in syenogranite is sodic-calcic amphibole, whereas that in peralkaline granite is sodic amphibole. On the $(Al + Fe^{3+}+2Ti)^{C}$ vs. $(Na + K + 2Ca)^{A}$ diagram, the sodic-calcic amphibole is classified as katophorite (Fig. 7a). According to the classification scheme of Hawthorne et al. (2012), these analyses are mostly ferro-ferri-katophorite. On the Si vs. $Mg/(Mg + Fe^{2+})$ diagram (Fig. 7b), most of the analyzed sodic amphiboles plot as magnesio-arfvedsonite, which is also their formal classification according to Hawthorne et al. (2012).

5.2. Pyroxene

Pyroxene was analyzed in syenogranite and peralkaline granite; chemical compositions and structural formulae are given in Supplementary Table 2S. Low apparent probe totals are due to assuming total Fe as FeO when it is Fe_2O_3. All the pyroxene analyses are Na-rich and

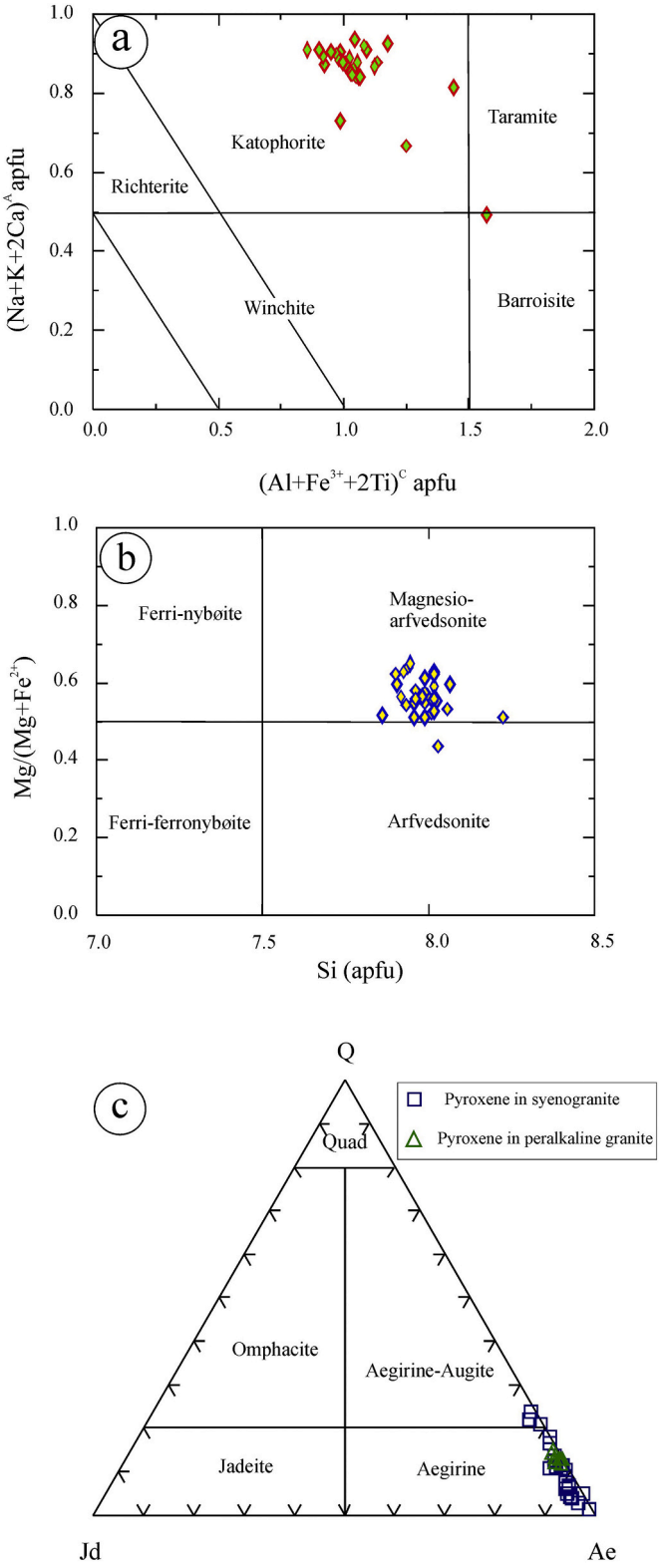

Fig. 7. (a) Plot of amphiboles analyses on the sodium-calcium amphiboles classification diagram (after Hawthorne et al., 2012). (b) Classification of the sodic amphiboles (after Hawthorne et al., 2012), this diagram applies only to sodic amphiboles (Na/(Na + Ca) on B site > 0.75) with $Fe^{3+}/(Fe^{3+} + Al)$ on the C site > 0.5 and Na on the A site > 0.5. (c) Plot of Na pyroxenes in the Q-Jd-Ae ternary diagram (Morimoto et al., 1988).

dominated by Fe_2O_3 over Al_2O_3; they are classified mainly as aegirine with a few points in syenogranite being aegirine-augite (Fig. 7c). All aegirine analyses are almost silica saturated (Si = ~ 2.00), with no significant substitution on tetrahedral sites (Abdel-Karim et al., 2021).

5.3. Pyroxmangite

Chemical compositions and structural formulae based on 6 oxygens for pyroxmangite from white pegmatite are given in Supplementary Table 3S. The analyses are dominated by SiO_2 (44.9–46.7 wt%), FeO* (11.9–23.1 wt%), and MnO (28.3–41.5 wt%). Minor CaO (0.41–1.3 wt %) is present; all other oxides are negligible. EDS spectra of pyroxmangite reveal minor concentrations of ZnO (~0.8 wt%) and Sc_2O_3 (~0.3 wt%), not analyzed by EPMA (Fig. 8a, b).

Distinguishing between pyroxmangite and rhodonite is difficult due to the close similarity between their structures, both belonging to the pyroxenoid group. There are published reports of the two minerals occurring together as bladed intergrowths (e.g., Michailidis and Sofianska, 2010; Millsteed et al., 2005; Pinckney and Burnham, 1988). However, typical rhodonite contains more than 5.0 wt% CaO (Caucia et al., 2020), whereas pyroxmangite generally has very low CaO, like the present analyses.

Moreover, the Raman spectra of the two phases are distinct (RRUFF.info). The Raman spectra of the of the Aja material are only consistent with pyroxmangite and not with rhodonite (Fig. 8c): the peak at 700 cm^{-1} (unique to pyroxmangite) is present, whereas the two peaks at 940

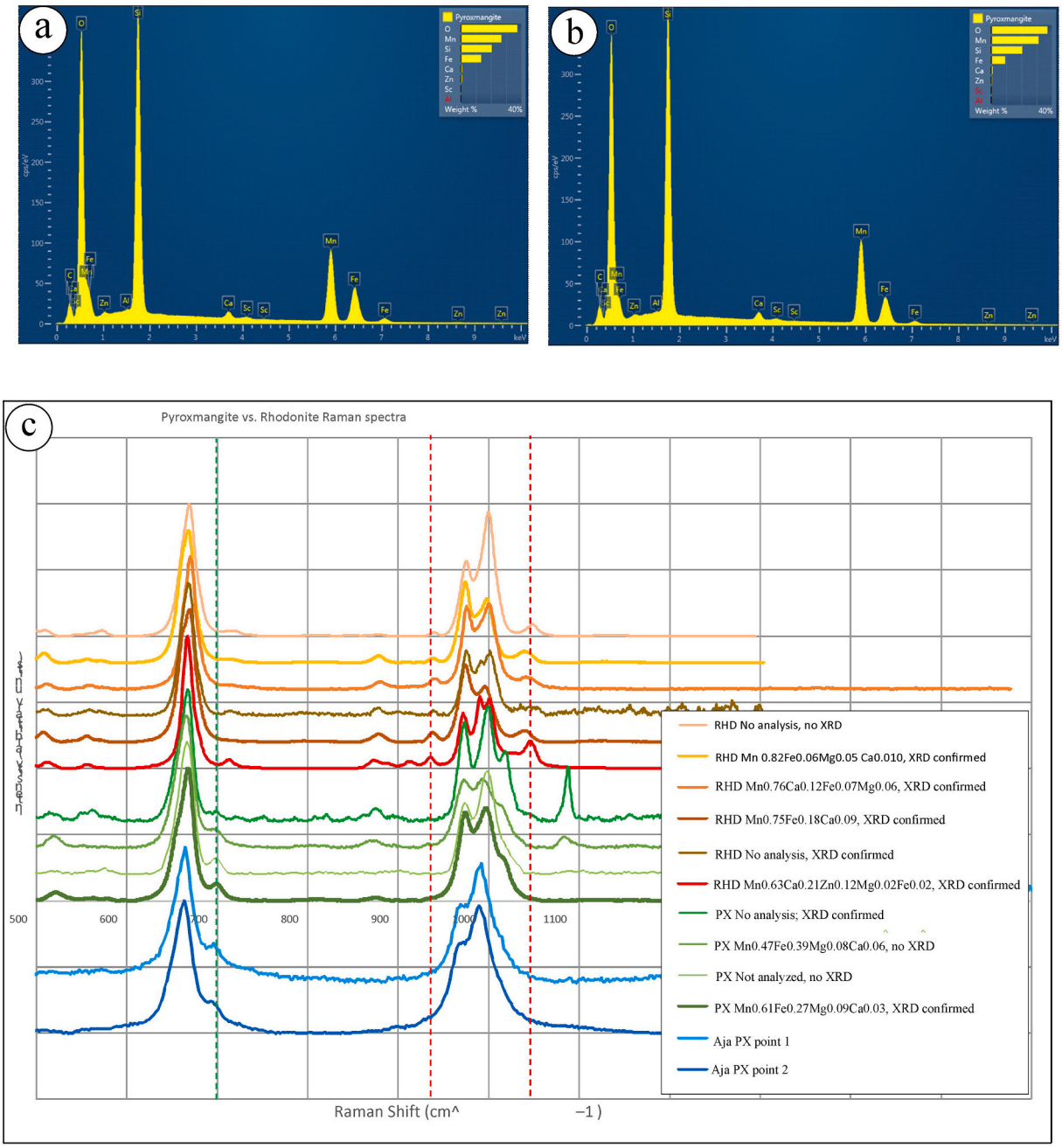

Fig. 8. (a, b) EDS spectra from two points in pyroxmangite. (c) Normalized Raman spectra, offset for clarity, supporting the assignment of $MnSiO_3$ to pyroxmangite rather than rhodonite; two Jebel Aja sample spectra are shown at bottom alongside several reference spectra from the RRUFF library. The peak marked in green (only in pyroxmangite) is present in the Jebel Aja samples, whereas the two peaks marked in red (only in rhodonite) are missing from the Jebel Aja samples. (For interpretation of the references to color in this figure legend, the reader is referred to the web version of this article.)

and 1050 cm^{-1} (unique to rhodonite) are absent.

5.4. Garnet

Garnet was analyzed only in the pyroxmangite-bearing pegmatite sample; chemical analyses, structural formulae and end member fractions are given in Supplementary Table 4S. All the analyzed garnets are spessartine (51.2–77.6 mol%), with almandine (14.5–44.2 mol%) being the second most abundant component and other components (grossular 2.3–6.3 mol%; pyrope <0.9 mol%; and andradite <0.5 mol%) being very minor. The identification of garnet was confirmed by EBSD and Raman spectroscopy (Fig. 9a), which also reveals prominent peaks

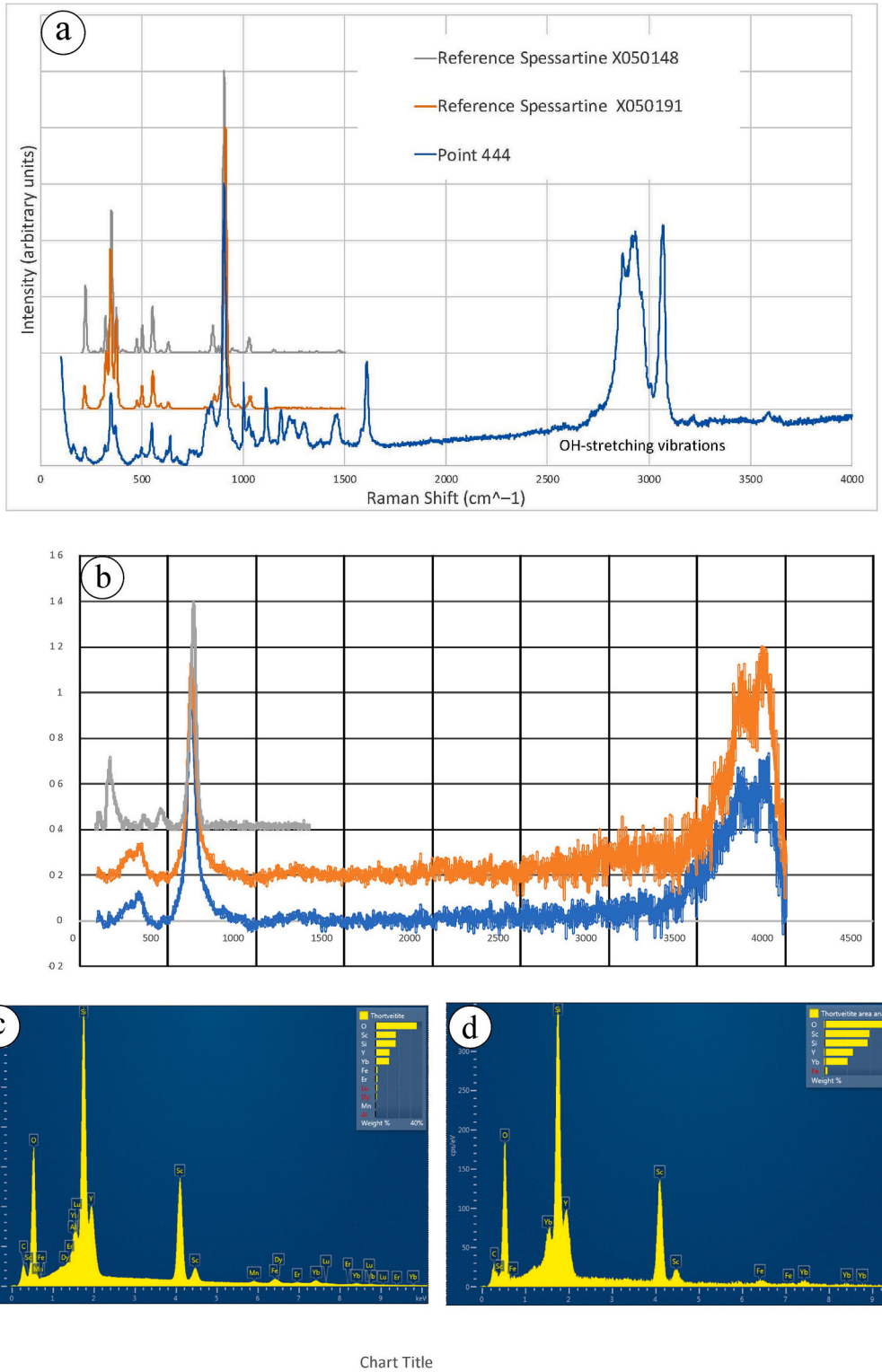

Fig. 9. (a) Normalized Raman spectra, offset for clarity, comparing hydrospessartine garnet in Jebel Aja pyroxmangite-bearing sample to reference spectra from the RRUFF library. (b) Normalized Raman spectra, offset for clarity, comparing two points on pyrochroite to a reference spectraum from the RRUFF library, and (c, d) EDS spectra from two points in thortveitite.

in the OH-stretching region. This confirms that low analytical totals observed in many garnet points are not due to poor focus or ferric iron but to hydrospessartine substitution. Points with analytical totals ≤99 wt% are assigned to hydrospessartine. The observed garnet compositions are similar to those commonly crystallized from hydrous, silicic magma at low pressure (Azer et al., 2020; Patiño Douce, 1999; Sami et al., 2020).

5.5. Feldspars

Feldspars were analyzed in syenogranite, peralkaline granite and pyroxmangite-bearing white pegmatite. Chemical compositions, structural formulae, and end-member components are given in Supplementary Tables (S5, S6). Only albite was found in the pyroxmangite sample. Syenogranite contains K-feldspar, anorthoclase, and albite. Peralkaline granite contains K-feldspar and albite.

5.6. Muscovite

A few muscovite crystals were analyzed in the pyroxmangite-bearing pegmatite sample; chemical compositions and structural formulae are given in Supplementary Table 7S. The analyzed muscovite crystals have low TiO_2, MgO and Na_2O contents, which are characteristic of secondary muscovite (Seddik et al., 2020; Villa et al., 1997), as expected from textural observations.

5.7. Pyrochroite

A MnO-dominant phase with low probe totals was observed in the pyroxmangite-bearing pegmatite sample. Raman spectroscopy confirmed that this mineral is pyrochroite (Fig. 9b) and also confirmed the presence of abundant structural water, explaining the low totals. Quantitatively analysis by electron microprobe reveals dominantly MnO; structural formulae were computed on the assumption of 2H atoms and 2 O atoms per formula unit (Supplementary Table 8S).

5.8. Fluorite

Fluorite was analyzed only in the pyroxmangite-bearing pegmatite. Fluorine was not analyzed, so the totals are low and the apparent composition is entirely dominated by CaO (Supplementary Table 9S). Additional analyses by SEM/EDS indicate the presence of a Y-bearing variety of fluorite as well as inclusions of thalénite-(Y) within fluorite.

5.9. Iron-titanium oxides

Magnetite, ilmenite, rutile and goethite are the main Fe-Ti oxides found as accessory phases in the AJII samples. Microprobe analyses and structural formulae of magnetite, observed in syenogranite and in pyroxmangite-bearing pegmatite, are given in Supplementary Table 10S. All the magnetite found in association with pyroxmangite is almost pure Ti-free magnetite ($TiO_2 \leq 0.15$ wt%), whereas syenogranite contains Ti-bearing magnetite with TiO_2 contents between 1.95 and 9.02 wt%.

Ilmenite was analyzed in syenogranite and peralkaline granite; chemical compositions and structural formulae are given in Supplementary Table 11S. In the syenogranite, although only two ilmenite analyses were collected, it is clear that the material is close to end-member ilmenite, with high TiO_2 (50.2–50.6 wt%) and FeO* (46.6–47.0 wt%) contents and low MnO contents (1.41–1.85 wt%). On the other hand, ilmenite in peralkaline granite is very rich in MnO (4.4–23.5 wt%) with a complementary depletion in FeO (21.5–40.1 wt %). We label this material "Mn-ilmenite". It contains 10 to 35 mol% pyrophanite ($MnTiO_3$) component (except for one point with 51.1 mol% pyrophanite that is therefore pyrophanite sensu stricto), a common substitution in oxidizing granitic rocks (Deer et al., 1992). We note also that the majority of these analyses have apparently >1 atom of Ti (up to 1.105) per 3-oxygen formula unit (apfu). Although ilmenite analyses with <1 apfu of Ti may be explained by solid solution towards hematite, the complementary case is rare. It may suggest incipient alteration towards rutile via the pseudorutile pathway (Grey and Reid, 1975).

Because syenogranite sample Aj26 contains both magnetite and ilmenite, it may be possible to apply two-oxide oxygen thermobarometry to this sample. However, the magnetite in this rock is low and variable in TiO_2, 5.63 ± 2.43 wt% and the ilmenite has very low hematite component. These compositions plot just on the edge of the calibrated range of published two-oxide oxygen thermobarometers at low pressure. However, attempting to use the calibration of Sauerzapf et al. (2008) yields $T \sim 600$ °C and $fO_2 \sim$ NNO + 1. This result may be qualitatively interpreted to indicate either (a) that the oxide phases in syenogranite crystallized very late in the petrogenesis, from an oxidized, low-temperature, residual melt or (b) that the oxide phases re-equilibrated in the subsolidus, leading to decrease in TiO_2 from the magnetite and loss of Fe_2O_3 from the ilmenite.

Rutile is a common accessory mineral in the peralkaline granite and an occasional one in the syenogranite; microprobe analyses of rutile are given in Supplementary Table 12S. The analyzed rutile is nearly pure TiO_2; the most significant other oxide present above detection level is FeO* (average 0.83 wt%, maximum 2.1 wt%).

Goethite is a common alteration mineral in the syenogranite and rarely in the peralkaline granite; microprobe analyses of goethite are given in Supplementary Table 13S. Totals for this hydrous and often porous phase are low. FeO* (>58.6 wt%) is the main constituent, alongside variable but ubiquitous SiO_2 (3.8–13.0 wt%). It is likely that this material is a fine-grained aggregate of more than mineral, but the Raman spectra support the assignment to dominantly goethite.

5.10. Thortveitite

Thortveitite is nominally $(Sc,Y)_2Si_2O_7$. In the pyroxmangite-bearing pegmatite sample, thortveitite occurs as small lath-shaped crystals with zonation, adjacent to magnetite within the cleavage-plane quartz-magnetite veins in pyroxmangite crystals. Its presence was first recognized by an automated Raman spectrum library search, confirmed by EBSD. A custom electron microprobe protocol was developed to analyze the long list of elements visible at appreciable concentrations in EDS spectra of this mineral, which in addition to the elements in the nominal formula also contains appreciable substitution of Yb and other heavy rare earth elements (Fig. 9c, d). Electron probe results and ions per 7-oxygen formula unit are given in Supplementary Table 14S. In addition to the dominant SiO_2 and Sc_2O_3 components, the analyzed thortveitite contains 5.5–6.8 wt% Y_2O_3, 5.9–7.2 wt% Yb_2O_3, and 4.7–5.4 wt % of the other analyzed REE oxides (Sm, Gd, Dy, Ho, Er, and Lu).

5.11. Thalénite-(Y)

Thalénite-(Y) is nominally $Y_3Si_3O_{10}F$. In the pyroxmangite-bearing pegmatite sample, thalénite-(Y) occurs in fluorite within the cleavage-plane quartz-magnetite veins in pyroxmangite crystals. Its presence was first recognized by EDS analysis and its structure confirmed by EBSD. Electron probe results and ions per 10-oxygen formula unit are given in Supplementary Table 14S. In addition to the stoichiometric components of the nominal formula, the analyzed thalénite-(Y) contains 18.4–19.9 wt% of the other analyzed REE oxides (Sm, Gd, Dy, Ho, Er, Yb, and Lu).

5.12. Mn oxides

Mn oxides are recorded in syenogranite and in pyroxmangite-bearing pegmatite. Energy-dispersive X-ray spectra of Mn oxide in syenogranite are shown Fig. 10a, b. Another phase of Mn-rich silicate with much higher apparent Mn/Si ratio than pyroxmangite, according to 10 kV EDS

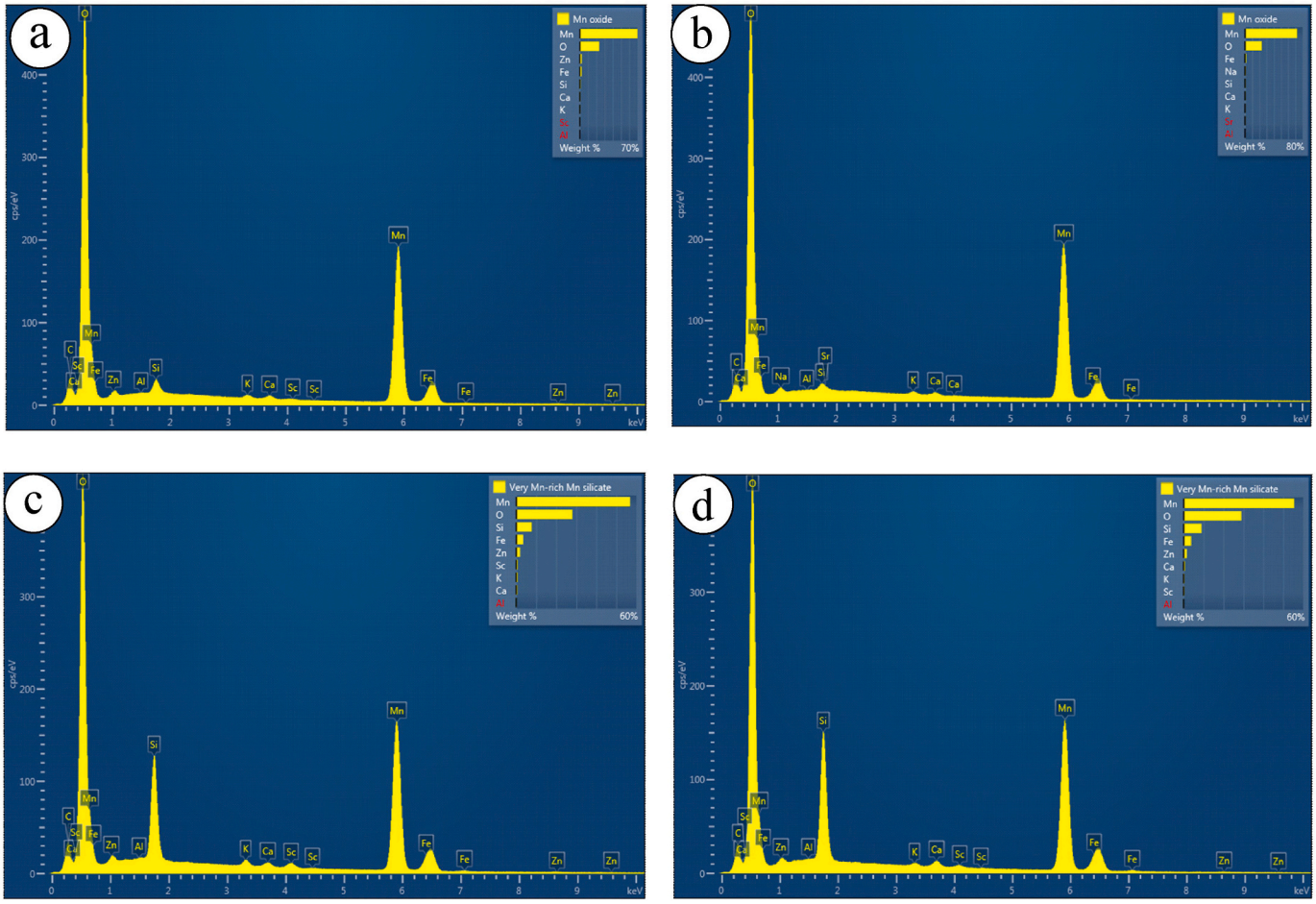

Fig. 10. (a, b) EDS spectra from two points in Mn oxide. (c, d) EDS spectra from two points on tiny hausmannite grains contaminated by counts form adjacent silicates.

analyses, was found in pyroxmangite-bearing pegmatite sample (Fig. 10c, d). However, the grains are extremely small (<1 μm) and we suspect that this phase is hausmannite (Mn_3O_4), contaminated by Si count due to secondary fluorescence from adjacent silicates.

5.13. Sc-rich pyroxenes

In the quartz-magnetite veins filling the cleavage planes in pyroxmangite, there are numerous laths of a (Sc, Mn, Fe)-silicate and a (Ca, Sc, Mn, Fe)-silicate. These phases were analyzed for general composition and structure by EDS and EBSD on the field-emission SEM (Fig. 11a, b, c, d) and for detailed composition with a customized electron microprobe protocol. Electron probe results and ions per 6-oxygen formula unit are given in Supplementary Table 14S. The (Sc, Mn, Fe)-rich phase has a triclinic structure and an average formula of $(Ca_{0.03}Sc_{0.27}Mn_{1.01}Fe_{0.44}Y_{0.02}Yb_{0.02})_{\Sigma 1.79}Si_{2.02}O_6$; it appears to be a (Sc, Y, Yb)-bearing, highly-defective, vacancy-rich variety of pyroxmangite. The (Ca, Sc, Mn, Fe)-rich phase is a monoclinic clinopyroxene with formula $(Ca_{0.47}Sc_{0.18}Fe_{0.14}Y_{0.01}Yb_{0.01})_{\Sigma M2=0.81}(Mn_{0.68}Fe_{0.26}Si_{0.06})_{\Sigma M1=1.00}Si_2O_6$. Although closer to the ideal formula of bustamite ($CaMnSi_2O_6$) than it is to any other named pyroxene species, this material is exotic and highly defective. It has substantial vacancies on the M2 site and excess Si accommodated on the M1 site. These crystal chemical features are most commonly found in high-pressure pyroxenes (Angel et al., 1988; Day and Mulcahy, 2007; Fockenberg and Schreyer, 1997; Ma et al., 2015, 2021; Wood and Henderson, 1978).

5.14. Apatite

Partial chemical analyses of apatite in the syenogranite and peralkaline granite are presented in Supplementary Table 15S. Fluorine and chlorine were not analyzed and so these analyses are incomplete. Although CaO and P_2O_5 are the major detected oxides, as expected, there is also significant Na_2O (1.1–2.5 wt%) and totals much lower than can be accounted for by the presence of hydroxyl, fluorine, or even chlorine on the anion site of apatite. It is likely that there is significant carbonate substituting for phosphate in this material, as is common in biomineralized hydroxyapatite (Nelson and Featherstone, 1982).

6. Geochemistry

6.1. Geochemical characteristics

Whole-rock geochemical analyses are provided for 15 samples representing the syenogranite, alkaline/peralkaline granites and pegmatites. Major oxides and calculated CIPW norms are given in Table 1, trace element concentrations in Table 2, and rare-earth elements with selected normalized REE rations in Table 3. Although all samples are high-SiO_2 granitoids, there is a distinction between the SiO_2 contents of the pegmatites (74.1–76.2 wt%) and the other samples (72.5–74.2 wt%). Using the R_1-R_2 diagram of De la Roche et al. (1980), all samples plot in the alkali granite field (Fig. 12), which is consistent with the petrographic description of the samples. With increasing SiO_2, concentrations of TiO_2, Al_2O_3, MgO, and CaO decrease, whereas Fe_2O_{3t} and MnO show a scattered increase and total alkali content ($Na_2O + K_2O$) is nearly constant

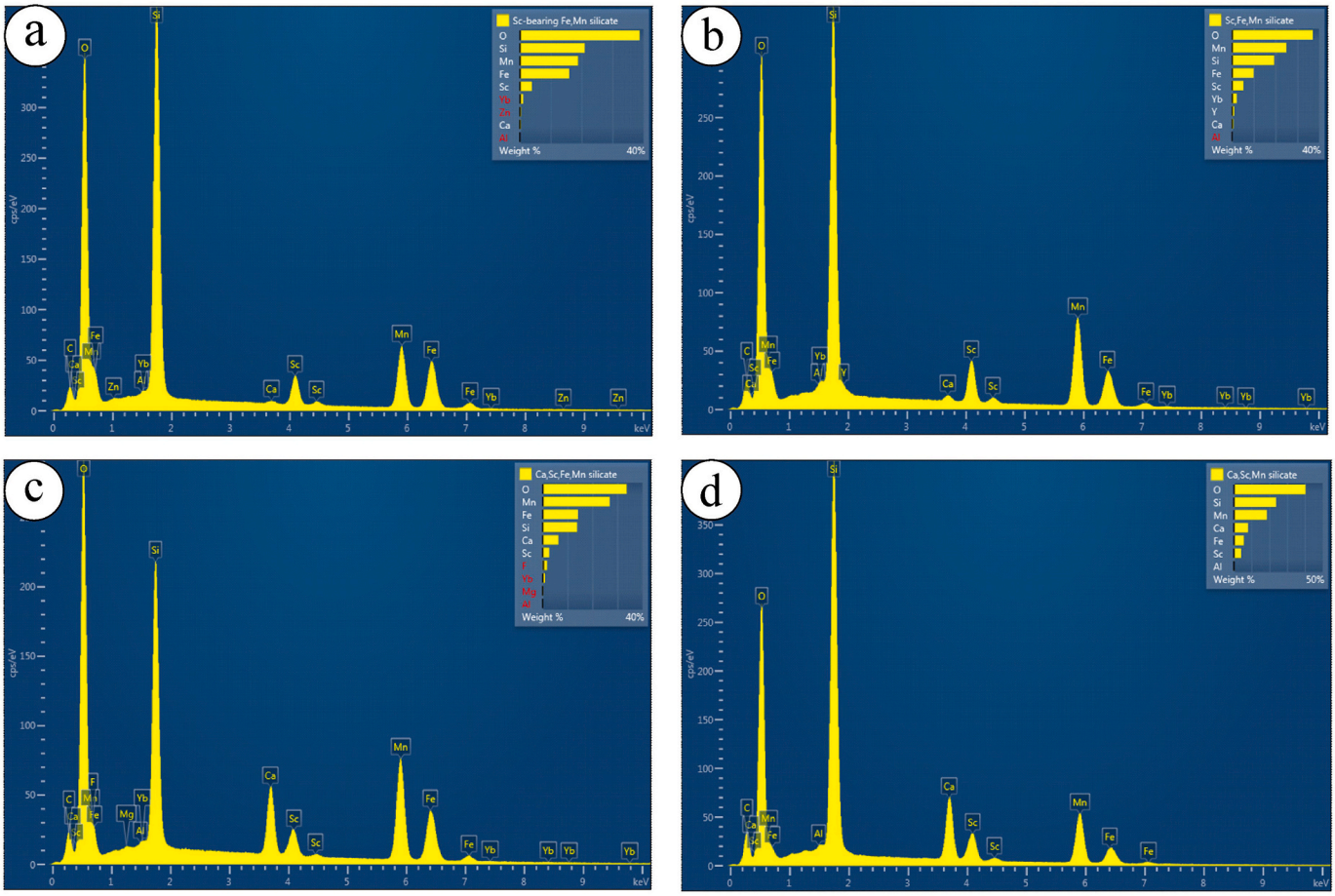

Fig. 11. (a, b) EDS spectra from two points on a (Sc, Yb)-bearing variety of pyroxmangite. (c, d) EDS spectra from two points on Sc-bearing, excess-Si bustamite.

Table 1
Major oxides and normative compositions (wt%) of JAII samples.

Rock type	Syenogranite				Alkaline granite			Peralkaline granite			White pegmatite		Pink pegmatite		
Sample	Aj18	Aj26	Aj33	Aj40	Aj13	Aj14	Aj8	Aj16	Aj5	Aj9	Aj21	Aj24	Aj23	Aj30	Aj36
SiO_2	72.56	72.54	74.08	73.05	73.03	73.57	72.56	73.33	73.06	74.18	74.06	74.05	76.22	75.48	74.66
TiO_2	0.27	0.28	0.21	0.25	0.27	0.23	0.25	0.21	0.25	0.19	0.14	0.18	0.13	0.09	0.12
Al_2O_3	11.92	12.18	10.56	12.46	10.46	11.75	11.83	11.23	10.22	10.06	11.14	10.65	8.58	9.41	10.15
Fe_2O_3	3.63	3.23	4.54	3.05	4.47	3.46	3.4	4.01	4.76	4.19	3.64	4.14	4.69	4.46	4.52
MnO	0.06	0.06	0.07	0.05	0.07	0.04	0.06	0.07	0.07	0.09	0.05	0.06	0.11	0.08	0.07
MgO	0.22	0.17	0.18	0.24	0.17	0.2	0.24	0.21	0.16	0.13	0.14	0.16	0.12	0.12	0.16
CaO	0.62	0.58	0.54	0.56	0.55	0.53	0.53	0.51	0.53	0.51	0.47	0.49	0.45	0.45	0.47
Na_2O	4.76	4.73	4.54	4.52	4.86	5.31	5.43	5.21	4.79	4.49	5.92	5.37	3.16	3.85	3.89
K_2O	4.75	4.83	4.45	4.8	4.78	4.48	4.77	4.46	4.68	4.5	3.38	3.54	5.28	4.86	4.98
P_2O_5	0.03	0.04	0.01	0.04	0.02	0.02	0.04	0.03	0.01	0.01	0.02	0.02	0.04	0.04	0.04
LOI	0.53	0.84	0.27	0.67	0.35	0.59	0.44	0.91	0.41	0.65	0.78	0.67	0.81	0.62	0.71
Total	99.482	99.48	99.76	99.81	99.61	100.16	99.55	100.22	99.67	99.93	99.54	99.41	99.53	99.45	100.01
Quartz	26.44	26.13	31.75	26.33	30.67	27.66	26.21	28.63	31.34	33.94	30.18	31.74	40.83	37.28	33.94
Orthoclase	28.49	29.01	26.63	28.72	28.73	26.67	28.52	26.63	28.17	27.13	20.25	21.28	31.73	29.17	29.82
Albite	35.37	36.32	29.89	37.81	27.64	35.73	34.67	33.25	26.99	27.22	38.98	35.65	14.97	21.66	24.79
Acmite	1.75	1.58	2.12	0.81	2.13	1.63	1.63	1.88	2.25	1.98	1.69	1.94	2.18	2.04	2.07
Na-Metasilicate	0.82	0.6	1.54	–	2.74	1.79	2.32	2.13	2.73	2.16	2.3	1.95	2.27	2.12	1.45
Diopside	2.56	2.33	2.16	2.22	2.33	2.12	2.09	2.25	2.44	2.22	1.97	2.06	1.6	1.77	1.85
Hypersthene	3.96	3.37	5.48	3.19	5.18	3.91	3.96	4.75	5.56	4.94	4.31	4.98	6.08	5.68	5.74
Magnetite	–	–	–	0.33	–	–	–	–	–	–	–	–	–	–	–
Ilmenite	0.52	0.54	0.4	0.48	0.52	0.44	0.48	0.4	0.48	0.37	0.27	0.35	0.25	0.17	0.23
Apatite	0.07	0.09	0.02	0.09	0.04	0.04	0.09	0.07	0.02	0.02	0.04	0.04	0.09	0.09	0.09
Color Index	7.04	6.25	8.04	6.23	8.03	6.47	6.53	7.4	8.48	7.53	6.55	7.39	7.93	7.63	7.82
Diff. Index	90.3	91.47	88.27	92.86	87.04	90.05	89.41	88.51	86.5	88.29	89.41	88.67	87.52	88.1	88.55
AI	1.09	1.07	1.16	1.01	1.26	1.16	1.19	1.19	1.27	1.22	1.20	1.19	1.27	1.23	1.16
ASI	0.84	0.87	0.80	0.91	0.74	0.81	0.78	0.78	0.73	0.76	0.78	0.78	0.73	0.76	0.80

Table 2
Trace element contents (μg/g) of JAII samples.

Rock type	Syenogranite				Alkaline granite			Peralkaline granite			White pegmatite		Pink pegmatite		
Sample	Aj18	Aj26	Aj33	Aj40	Aj13	Aj14	Aj8	Aj16	Aj5	Aj9	Aj21	Aj24	Aj23	Aj30	Aj36
Sc	2.26	2.68	1.71	2.47	2.03	1.53	2.03	1.85	2.12	1.75	20.27	16.59	34.13	32.9	27.5
V	12.15	17.58	6.22	11.55	6.99	5.24	10.72	7.67	6.65	2.55	11.72	8.01	27.5	22.86	20.86
Cr	2.03	2.69	1.62	2.33	2.81	2.41	2.48	1.34	3.06	1.83	1.12	6.43	1.04	0.67	0.92*
Co	26.34	28.66	26.61	22.9	27.59	21.67	21.69	24.33	32.14	22.47	1.4	12.61	1.51	1.05	1.21
Ni	4.12	3.53	1.78	3.21	2.76	2.52	2.77	2.49	2.78	2.23	2.87	2.43	5.96	3.4	2.7
Cu	8.47	8.18	6.08	6.45	7.97	7.26	7.85	8.3	6.23	5.71	11.52	7.33	60.38	34.75	30.61
Zn	121.5	192.54	226.13	139.62	265.41	156.81	142.33	184.81	334.17	251.12	252.1	235.49	738.13	599.26	537.23
Ga	34.12	30.19	36.78	32.87	36.52	37.01	34.68	37	36.53	41.95	44.35	44.91	38.9	38.93	44.43
Rb	194.43	176.01	251.42	194.54	216.22	237.78	215.02	279.47	234.88	284.83	362.72	340.17	344.3	312.2	295
Sr	73.22	66.98	48.13	73.95	35.36	40.14	46.36	27.33	26.99	25.21	20.85	21.04	16.71	18.71	19.35
Y	62.12	53.99	76.19	64.12	117.6	116.74	119.42	164.83	129.07	208.38	520.9	544.26	1616.1	1116.16	1291.56
Zr	717.04	616.96	964.8	544.95	1179.24	1021.54	1000.46	1092.84	1272.22	1266.62	4194.32	4260.85	9707.45	6391.98	8619.31
Nb	87.73	71.61	86.8	83.32	105.23	96.66	103.15	132.6	126.62	143.52	260.67	244.97	1768.58	1539.58	1578.85
Ba	155.73	120.77	83.12	152.28	74.87	89.89	108.99	76.66	62.99	46.23	66.42	99.63	32.06	48.8	67.2
Hf	19.57	20.79	24.64	18.81	29.43	26.49	25.79	32.82	33.7	34.38	106.7	109.84	263.95	214.98	251.11
Ta	3.29	3.97	3.51	3.67	5.97	6.92	7.24	10.27	5.79	9.67	59.65	47.36	135.98	109.31	103.25
Pb	17.51	17.04	22.92	17.34	27.53	24.98	29.04	49.66	35.09	51.41	27.7	36.45	362.23	286.93	260.66
Th	14.63	14.7	10.69	13.56	20.13	23	21.36	26.27	47.59	32.55	83.12	89.69	367.15	278.11	383.81
U	5.81	5.57	4.21	4.37	7.95	8.24	8.05	10.98	10.62	11.25	20.1	17.24	147.11	109.65	122.51
Sn	8.33	2.57	4.23	5.3	9.92	8.95	10.64	16.11	14.33	17.84	15.65	16.73	100.95	104.41	120.51
Cs	8.98	2.19	0.85	1.43	2.82	7.15	2.86	2.51	2.42	41.63	3.07	2.37	45.06	32.03	24.93

Table 3
Rare earth element contents (μg/g) of JAII samples.

Rock type	Syenogranite				Alkaline granite			Peralkaline granite			White pegmatite		Pink pegmatite		
Sample	Aj18	Aj26	Aj33	Aj40	Aj13	Aj14	Aj8	Aj16	Aj5	Aj9	Aj21	Aj24	Aj23	Aj30	Aj36
La	35.98	32.97	50.49	23.59	56.82	73.88	82.14	120.84	108.94	152.51	257.44	294.35	442.88	339.65	468.27
Ce	79.62	71.36	101.65	51.03	121.91	152.63	180.94	270.71	227.13	339.98	574.32	657.41	1035.74	796.28	1109.75
Pr	10.24	9.21	12.5	6.67	15.59	19.76	23.48	34.09	30.66	43.33	74.64	81.53	126.34	97.92	136.69
Nd	40.39	35.06	48.49	26.54	61.19	75.57	98.06	130.41	121.51	172.08	312.85	353.6	511.06	418.91	542.02
Sm	9.68	7.94	11.23	5.69	14.02	17.81	23.31	28.22	23.84	35.81	78.78	85.24	130.01	104.28	141.92
Eu	0.75	0.64	0.85	0.45	0.94	1.03	1.48	1.38	1.35	2.01	3.72	4.17	6.79	5.35	7.44
Gd	8.07	7.13	10.22	4.44	12.95	11.19	20.26	25.01	21.62	34.86	92.9	111.67	183.33	138.12	206.6
Tb	1.31	1.14	1.66	0.66	2.07	1.83	3.23	3.66	3.24	5.31	15.5	17.84	30.96	23.07	34.37
Dy	7.74	7.03	10.29	3.94	12.71	10.87	20.22	20.71	18.41	30.67	98.71	115.94	206.87	153.51	225.11
Ho	1.52	1.53	2.16	0.83	2.61	2.12	4.16	3.98	3.62	6.02	21.12	24.69	44.41	33.59	49.12
Er	4.11	4.39	6.14	2.38	7.43	6.21	11.71	11.51	10.39	16.05	59.34	70.13	126	96.62	143.07
Tm	0.59	0.65	0.92	0.38	1.11	0.94	1.78	1.69	1.52	2.23	9.05	10.48	19.21	14.78	21.52
Yb	4.13	4.61	6.06	2.78	7.38	6.09	11.91	10.82	9.97	14.75	59.35	70.11	127.19	97.32	142.95
Lu	0.65	0.71	0.93	0.47	1.11	0.93	1.78	1.61	1.49	2.22	9.05	10.63	19.46	14.88	21.98
ΣREE	204.78	184.37	263.59	129.85	317.84	380.86	484.46	664.64	583.69	857.83	1666.77	1907.79	3010.25	2334.28	3250.81
Eu/Eu*	0.26	0.26	0.24	0.27	0.21	0.22	0.21	0.16	0.18	0.17	0.13	0.13	0.13	0.14	0.13
(La/Yb)n	5.89	4.84	5.63	5.74	5.21	8.20	4.66	7.55	7.39	6.99	2.93	2.84	2.35	2.36	2.22
(La/Sm)n	2.35	2.62	2.84	2.62	2.56	2.62	2.22	2.70	2.88	2.69	2.06	2.18	2.15	2.06	2.08
(Gd/Lu)n	1.52	1.23	1.35	1.16	1.43	1.47	1.39	1.90	1.78	1.92	1.26	1.29	1.15	1.14	1.15
(La/Lu)n	5.67	4.76	5.56	5.14	5.24	8.14	4.73	7.69	7.49	7.04	2.91	2.84	2.33	2.34	2.18

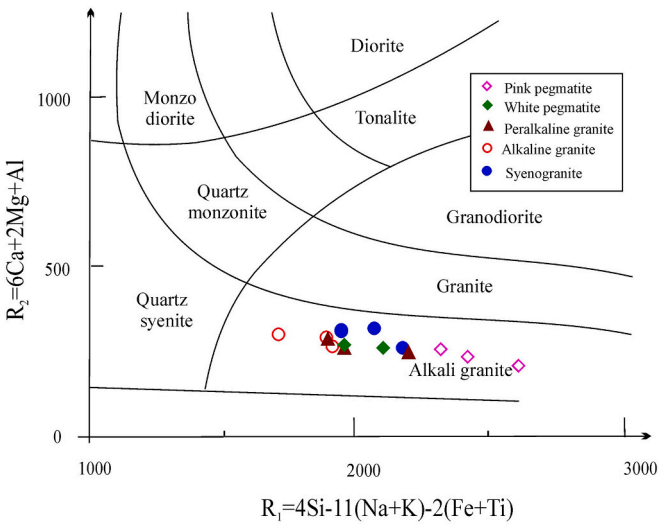

Fig. 12. Petrological classification of the Aja granites and pegmatites using the R_1-R_2 diagram of De la Roche et al. (1980).

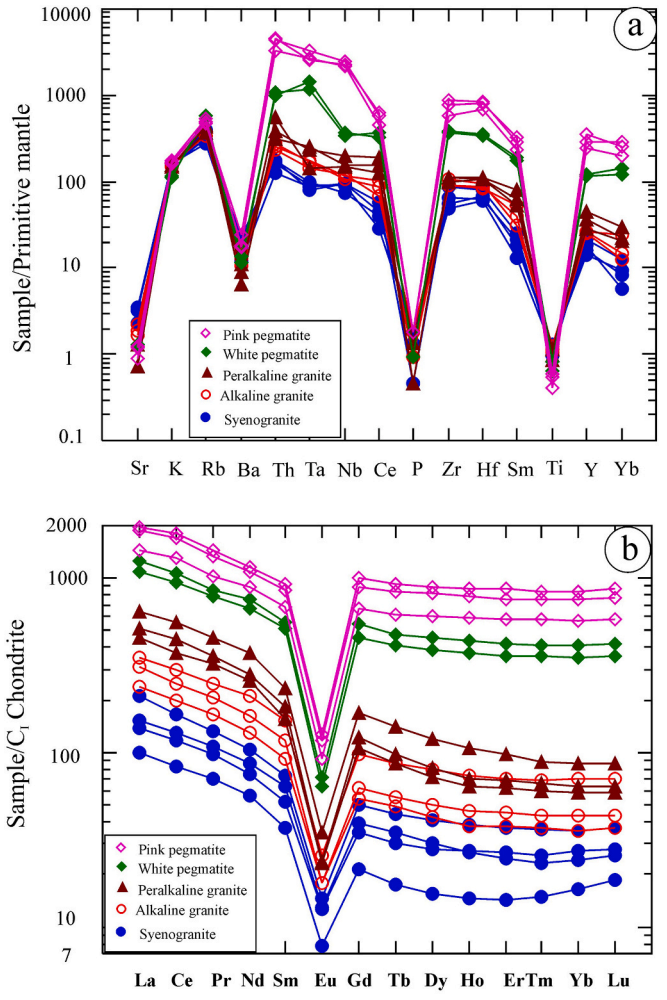

Fig. 13. (a) Primitive mantle-normalized extended trace element plots and (b) chondrite-normalized REE patterns for granite and pegmatites samples of the Jebel Aja Igneous Intrusion. Normalization values in (a) from Sun and McDonough (1989) and in (b) from Evensen et al. (1978).

(Table 1).

Although the trace element concentrations (Table 2) vary widely across the JAII sample suite, all the patterns share common features in the primitive-mantle (Sun and McDonough, 1989) normalized extended trace elements plot (Fig. 13a). Trace elements generally become progressively enriched in sequence from syenogranite through alkaline granite, peralkaline granite, white pegmatite, and pink pegmatite. Trace element concentrations exhibit extreme enrichments in the pegmatite samples, with very high abundances of Nb (≤1769 μg/g), Y (≤1616 μg/g), Ta (≤136 μg/g), Hf (≤264 μg/g), Th (≤384 μg/g), U (≤147 μg/g), Zr (≤9707 μg/g), Sn (≤121 μg/g) and Cs (≤45 μg/g). For purposes of tectonic discrimination and classification of the JAII, we will set aside the highly mineralized pegmatite samples.

The normalized trace-element patterns are characterized by enrichment in some large-ion lithophile elements (LILE: Rb, K, Th) and high field strength elements (HFSE: Ta, Nb, Zr, Hf), but strong depletions in Sr, Ba, P and Ti. This pattern is consistent with the geochemical signatures of A-type granites (Wu et al., 2002). The relative depletion in Sr, Ba, P and Ti are related to extensive fractionation of feldspars, apatite and Fe-Ti oxides, respectively (Bevins et al., 1995; Green, 1980).

There is an extreme range of REE contents in the granites and pegmatites of the JAII (Table 3). Total REE contents increase in sequence from syenogranite (ΣREE = 130–264 μg/g) through alkaline granite (ΣREE = 318–484 μg/g), peralkaline granite (ΣREE = 584–858 μg/g), and white pegmatite (ΣREE = 1668–1908 μg/g) to pink pegmatite (ΣREE = 2334–3251 μg/g). Again all samples show a number of common features in their chondrite-normalized REE patterns (Evensen et al., 1978) (Fig. 13b). All samples are enriched in light REE relative to heavy REE, but the magnitude of the fractionation decreases from the granites [$(La/Lu)_n$ = 4.73–8.14)] to the pegmatites [$(La/Lu)_n$ = 2.18–2.91]. The heavy REE display a prominent concave-up shape in syenogranite that fades with progressive evolution of the suite. If the concavity is the result of amphibole fractionation (Sisson, 1994), it apparently only affected the early evolution of the suite, at a stage more primitive than the erupted samples. The negative Eu anomalies are striking and increase in depth from syenogranite [$(Eu/Eu^*)_n$ = 0.24–0.26] to the pegmatites [$(Eu/Eu^*)_n$ = 0.13–0.14], indicating either early fractionation of plagioclase or residual plagioclase in the source of the syenogranite as well as continuing fractionation of feldspars across the sampled part of the suite. The depth of the negative Eu anomaly is correlated with the depth of Ba depletion. The negative Eu anomaly requires conditions sufficiently reducing to stabilize some Eu^{2+} (Hanson, 1978; McKay, 1989).

6.2. *Magma type and tectonic setting*

According to the agpaitic index [AI = molecular (Na_2O + K_2O)/Al_2O_3], all the analyzed granite and pegmatite samples are in the alkaline or peralkaline category, with AI >1 (Liégeois et al., 1998; Liégeois and Black, 1987). The alkaline/peralkaline affinity of the suite is confirmed by presence of acmite (0.81–2.25 wt%) and Na-metasilicate (0.60–2.74 wt%) in the norms and by the visible abundance of sodic amphibole and sodic pyroxene in the modal mineralogy. Using the diagram of Sylvester (1989), which distinguishes between the different rock-types with SiO_2 > 68 wt%, the analyzed samples lie deep within the alkaline field (Fig. 14a). On the FeO_t/MgO vs. Ga/Al discrimination diagram of Whalen et al. (1987), all of the analyzed JAII samples plot well into the A-type granite field (Fig. 14b).

Our results from field relationships, petrography, mineral chemistry, and bulk chemistry all help to define the tectonic context of the JAII. Geochemical features of the JAII diagnostic of post-collisional A-type rocks include its high alkali contents; high $FeO^T/(FeO^T + MgO)$; marked enrichments in Nb, Ta, Y, Th, Hf, Zr and REE; and depletions in Ba, Sr, P, Sc, Eu, V and Co. Moreover, the chemical characteristics of the JAII are consistent with a within-plate tectonic setting: they have alkaline/peralkaline character; high alkali contents; marked depletion in CaO, MgO,

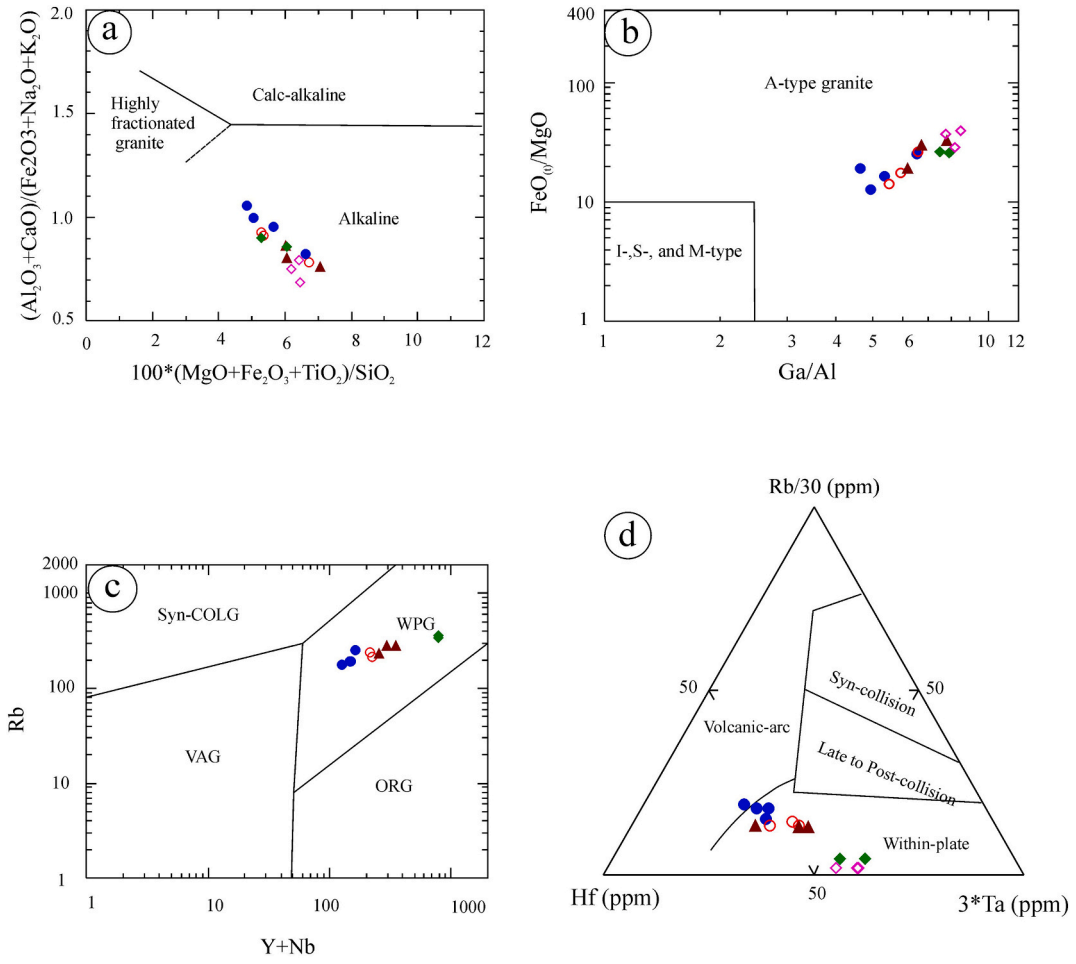

Fig. 14. Whole-rock geochemical and tectonic discrimination diagrams: (a) discrimination diagram of Sylvester (1989) for rocks with >68 wt% SiO_2, (b) Ga/Al vs. $FeO_{(t)}$/MgO diagram of Whalen et al. (1987), (c) Y + Nb vs. Rb (Pearce et al., 1984), and (d) Hf-Rb/30-3*Ta ternary diagram (after Harris et al., 1986). Symbols as in Fig. 12.

Sr, and transition metals; and primitive-mantle-normalized trace element patterns enriched in both LILE and HFSE with no anomalies in Nb or Ta (Pearce et al., 1984). On granitoid discrimination diagrams, the granites and pegmatites of JAII typically plot in the within-plate field (Figs. 14 c, d).

7. Discussion

7.1. Petrogenesis

Studies of the JAII published to date have drawn a diverse conclusion about its magmatic source and petrogenetic evolution, leaving considerable unresolved controversy (Abdallah et al., 2020; Abuamarah, 2020; Ekren et al., 1987; Hereher and Abdullah, 2017; Qadhi Talal, 2007; Stuckless et al., 1984). On the Rb/Nb vs. Y/Nb and Nb-Y-Ce diagrams of Eby (1990), the studied granitoid and pegmatite samples straddle the boundary between the A_1 and A_2 types that are thought to be associate with mantle and crustal sources, respectively (Fig. 15a, b). In fact, the two diagrams proposed by Eby (1990) yield contradictory results for most JAII samples. However, the absence of mafic lithologies in the JAII argues against an origin by fractional crystallization of mantle-derived mafic magma. As is generally the case for felsic plutons, a mantle-derived origin implies the presence of a mass of mafic cumulates complementary to and much larger than the felsic rocks themselves. There is no evidence for such cumulates. Accordingly, it seems most probably that the JAII has a crustal source, with a relatively evolved primary melt derived from partial melting of the juvenile continental crust of the ANS. The gneissic xenoliths in the syenogranite may be representative of the source region, and the mafic microgranular enclaves are likely to represent early cumulates from the fractionation sequence. In this context, the REE patterns of the syenogranites, the most primitive sampled members of the suite, with strongly concave up HREE, imply residual amphibole in the source and rule out residual garnet in the source. The disappearance of this concavity with progressive evolution of the suite argues against amphibole fractionation.

All chemical indicators point to the JAII rocks being cogenetic, with progressive differentiation from syenogranite through to white pegmatite. It is difficult in this case to infer whether the most primitive exposed syenogranite has already experienced fractional crystallization or whether it could be a primary melt of a plagioclase amphibolite. However, from syenogranite onwards, the trends are well-explained by progressive fractionation of feldspars, Fe-Ti oxides, and apatite. The break in slope in the trend of Rb/Sr against Sr (Fig. 15c) suggests a change from mostly plagioclase to mostly alkali feldspar fractionation between the alkaline and peralkaline segments of the suite, whereas the good correlations among Ba, Sr, CaO, and Eu/Eu* (Fig. 15d, e, f) confirm the importance of feldspar fractionation in controlling the evolution of the suite.

7.2. Interpretation of the pegmatites

Evidently, the trace element enrichment of the pegmatites, especially the pink pegmatites, reaches extraordinary levels. Although small in current outcrop area, they may be of interest for economic exploration

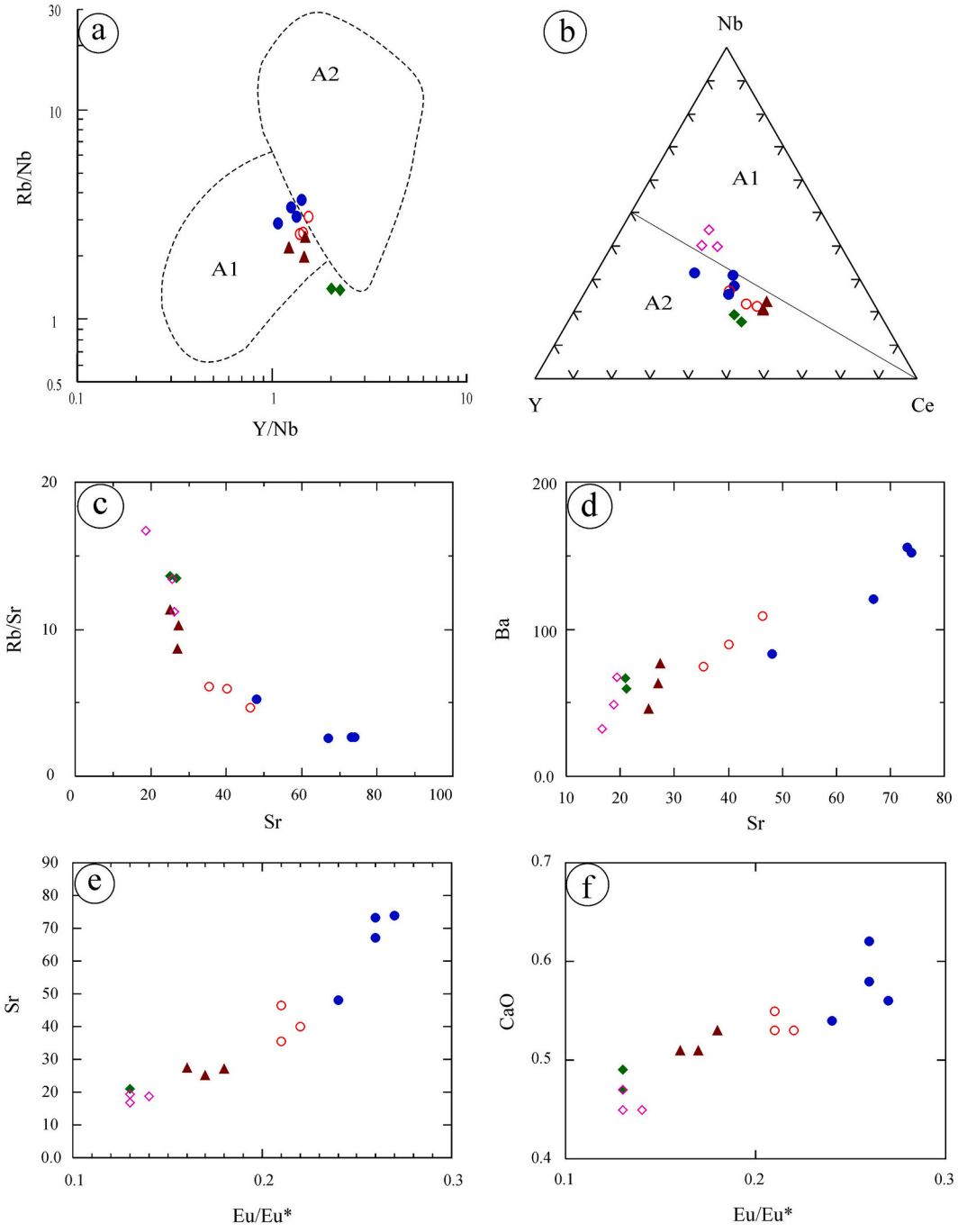

Fig. 15. Indicators of magmatic evolution: (a) Rb/Nb vs. Y/Nb diagram for distinction of A-type granitoids (Eby, 1992), (b) Nb-Y-Ce discrimination diagram of Eby (1992), A1 = A-type granitoids with an OIB-type mantle source, A2 = A-type granitoids with crustal sources, (c) Sr vs. Rb/Sr, (d) Sr vs. Ba, (e) Eu/Eu* vs. Sr concentration, and (f) Eu/Eu* anomaly vs. CaO. Symbols as in Fig. 12.

for REE, Y, Sc, Zr, Nb, Ta, etc. Here, however, we focus on the unusual mineralogy of the white pegmatite, especially the presence of Mn-rich phases and evidence for high-pressure crystallization.

The behavior of Mn during magmatic differentiation is strongly dependent on fO_2. Under reducing conditions where Mn is dominantly in the Mn^{2+} oxidation state, its behavior is similar to Fe^{2+} (Qin and Humayun, 2008). As higher oxidation states like Mn^{3+} and Mn^{4+} become stabilized, its behavior should diverge from that of Fe (e.g., Bromiley et al., 2015). In the present suite, MnO and Fe_2O_{3t} are well correlated, and both increase during differentiation, though in the whole-rock sample suite MnO only reaches a maximum of 0.11 wt%. The dominance of pyroxmangite, a Mn^{2+} mineral (with only a trace of hausmannite), in the mineralized white pegmatite sample and the only moderately oxidized fO_2 (NNO + 1) estimated for the more primitive part of the suite are consistent with accumulation of Mn^{2+} to the point of pyroxmangite saturation.

There are several indications in the pyroxmangite-bearing sample of a significantly elevated pressure of crystallization. First, pyroxmangite is the high-pressure dimorph of $MnSiO_3$, which forms rhodonite at low pressure. The equilibrium boundary between them, at a plausible temperature for pegmatite crystallization (≥500 °C), requires $P \geq 0.8$ GPa (Maresch and Mottana, 1976). Second, the novel vacancy-rich pyroxenoid and the novel vacancy-rich excess-Si pyroxene found in the cleavage planes of pyroxmangite both indicate substantially elevated

pressure (Angel et al., 1988; Day and Mulcahy, 2007; Fockenberg and Schreyer, 1997; Ma et al., 2015, 2021; Wood and Henderson, 1978), though their unique chemistry makes this impossible to quantify on the basis of currently available experiments. Such elevated pressure in a highly evolved granitoid in the Arabian Shield is surprising. Most exposed post-collisional A-type magmatic complexes in the Arabian Shield were emplaced at quite high crustal levels (Abdallah et al., 2020; Abuamarah et al., 2021). Many include volcanic and hypabyssal members. However, the AJII lies both on the very edge of the exposed Arabian Shield and at the center of the Shammar Basin. The Shammar Basin is interpreted by Genna et al. (2002) as the product of intracontinental extension and crustal thinning after 590 Ma. Primary structures associated with this extension include the Najd transform fault as well as normal faults that may be associated with core complexes, tilted blocks, and isostatic footwall uplifts (Lister and Davis, 1989). Although the JAII is undeformed and unmetamorphosed, the mineralogical evidence cited here suggests that it may have experienced substantial uplift and erosion to the current depth of exposure, at least in the southern part. Testing this suggestion requires further structural as well as mineralogical investigation.

8. Summary

We document the first known occurrence of pyroxmangite, the high-pressure dimorph of $MnSiO_3$, in the whole ANS, in a pegmatite associated with the Jebel Aja Igneous Intrusion. It is associated with an assemblage of Mn, Y, Sc, and REE ore minerals including thortveitite, spessartine, pyrochroite, thalénite-(Y), a novel (Sc, Y, vacancy)-rich variety of pyroxmangite, and a vacancy-rich bustamite with excess octahedral Si. The JAII consists of two consecutive but apparently cogenetic pulses of granitoid emplacement. The early, less fractionated phase is dominantly syenogranite. The later, more fractionated phase, emplaced underneath the early phase, consists of alkaline and peralkaline granites.

The whole suite is alkaline and A-type in character and post-collisional. White and pink pegmatites occur along the contact between syenogranite and alkaline/peralkaline granite. The pink pegmatites are the most enriched in trace elements, but the exotic Mn, Y, Sc, and REE minerals are found in a pocket in the white pegmatite. The presence of pyroxmangite and defective, vacancy-rich, Si-excess pyroxenes suggests a surprisingly high pressure of emplacement of this white pegmatite, which in turn suggests considerable uplift and erosion to reach the current exposure level of the southern JAII.

Declaration of Competing Interest

The authors declare that they have no known competing financial interests or personal relationships that could have appeared to influence the work reported in this paper.

Acknowledgements

The authors would like to extend their appreciation and gratitude to the Deanship of Scientific Research, King Saud University for funding and supporting this work through Research Group No. RG-1436-036. Analytical work at the Caltech GPS Division Analytical Facilities is partially supported by NSF Grants EAR-0318518 and DMR-0080065. PDA acknowledges NSF award 1911902. The authors highly appreciate thoughtful reviews by the two anonymous reviewers. In addition, the authors are also indebted to the editor (Prof. Michael Roden) for his efforts and numerous helpful comments.

Appendix A. Supplementary data

Supplementary data to this article can be found online at https://doi.org/10.1016/j.lithos.2021.106395.

References

Abdallah, S.E., Azer, M.K., Shammari, A.S., 2020. The petrological and geochemical evolution of Ediacaran rare-metal bearing A-type Granites from the Jabal Aja Complex, Northern Arabian Shield, Saudi Arabia. Acta Geol. Sin. Engl. Ed. 94 (3), 743–762.
Abdel-Karim, A.M., 1992. Fluorite granites from southwest Sinai of Egypt, with particular reference to the A-type. Acta Mineral. Petrogr. XXXIII 57–65.
Abdel-Karim, A.M., 1996. Petrogenesis of late Precambrian younger granites from southwest Sinai, Egypt. J. Mineral. Petrol. Econ. Geol. 91 (5), 185–195.
Abdel-Karim, A.M., Azer, M.K., Sami, M., 2021. Petrogenesis and tectonic implications of the Maladob ring complex in the South Eastern Desert, Egypt: new insights from mineral chemistry and whole-rock geochemistry. Int. J. Earth Sci. 110, 53–80.
Abuamarah, B.A., 2020. Genesis and petrology of post-collisional rare-metal-bearing granites in the Arabian Shield: a case study of Aja Ring Complex, Northern Saudi Arabia. J. Geol. 128 (2), 131–156.
Abuamarah, B.A., Azer, M.K., Asimow, P.D., Shi, Q., 2021. Petrogenesis of the post-collisional rare-metal-bearing Ad-Dayheen granite intrusion, Central Arabian Shield. Lithos 384, 105956.
Agar, R.A., 1992. The tectono-metallogenic evolution of the Arabian Shield. Precambrian Res. 58 (1–4), 169–194.
Ali, K.A., Azer, M.K., Gahlan, H.A., Wilde, S.A., Samuel, M.D., Stern, R.J., 2010. Age constraints on the formation and emplacement of Neoproterozoic ophiolites along the Allaqi-Heiani suture, South Eastern Desert of Egypt. Gondwana Res. 18, 583–595.
Angel, R.J., Gasparik, T., Ross, N.L., Finger, L.W., Prewitt, C.T., Hazen, R.M., 1988. A silica-rich sodium pyroxene phase with six-coordinated silicon. Nature 335 (6186), 156–158.
Azer, M.K., Gahlan, H.A., Asimow, P.D., Al-Kahtany, K.M., 2017. The late Neoproterozoic Dahanib mafic-ultramafic intrusion, South Eastern Desert, Egypt: is it an Alaskan-type or a layered intrusion? Am. J. Sci. 317, 901–940.
Azer, M.K., Abdelfadil, K.M., Asimow, P.D., Khalil, A.E., 2020. Tracking the transition from subduction-related to post-collisional magmatism in the north Arabian–Nubian Shield: a case study from the Homrit Waggat area of the Eastern Desert of Egypt. Geol. J. 55, 4426–4452.
Bevins, R.E., Pharaoh, T.C., Cope, J.C.W., Brewer, T.S., 1995. Geochemical character of Neoproterozoic volcanic rocks in southwest Wales. Geol. Mag. 132, 339–349.
Bromiley, G.D., Gatta, G.D., Stokes, T., 2015. Manganese incorporation in synthetic hercynite. Mineral. Mag. 79, 635–647.
Caucia, F., Marinoni, L., Riccardi, M.P., Bartoli, O., Scacchetti, M., 2020. Rhodonite-pyroxmangite from Tanatzalp, Switzerland. Gems Gemol. 56 (1).
Day, H.W., Mulcahy, S.R., 2007. Excess silica in omphacite and the formation of free silica in eclogite. J. Metamorph. Geol. 25 (1), 37–50.
De la Roche, H., Leterrier, J., Grandclaude, P., Marchal, M., 1980. A classification of volcanic and plutonic rocks using R_1-R_2 diagrams and major-element analyses-its relation with current nomenclature. Chem. Geol. 29, 183–210.
Deer, W., Howie, R., Zussman, J., 1992. An Introduction to the Rock Forming Minerals, Second edition. Longman Scientific and Technical, London. (696 pp.).
Drysdall, A.R., Douch, C.J., 1986. Nb–Th–Zr mineralization in microgranite – microsyenite at Jabal Tawlah, Midyan region, Kingdom of Saudi Arabia. J. Afr. Earth Sci. 4, 275–288.
Drysdall, A.R., Jackson, N.J., Douch, C.J., Ramsay, C.R., Hackett, D., 1984. Rare metal mineralization related to alkali granites in the Arabian Shield. Econ. Geol. 79, 1366–1377.
Eby, G.N., 1990. The A-type granitoids: a review of their occurrence and chemical characteristics and speculations on their petrogenesis. Lithos 26, 115–134.
Eby, G.N., 1992. Chemical subdivisions of the A-type granitoids: petrogenesis and tectonic implications. Geology 20, 641–644.
Ekren, E.B., Vaslet, D., Berthiaux, A., Strat, P.L., Fourniguet, J., 1987. Geologic Map of the Ha'il Quadrangle, Sheet 27E, Kingdom of Saudi Arabia, Deputy Ministry for Mineral Resources. Ministry of Petroleum and Mineral Resources, Kingdom of Saudi Arabia (Scale 1:250,000).
Elliott, J.E., Al-Yazidi, S., Al-Eissa, H., Al-Shammeri, A., Hashem, H.I., Tarabulsi, Y., 1999. Exploration of the Ghurayyah Radioactive Granite. Kingdom of Saudi Arabia, Saudi.
Evensen, N.M., Hamilton, P.J., O' Nions, R.K., 1978. Rare earth abundances in chondritic meteorites. Geochim. Cosmochim. Acta 42 (8), 1199–1212.
Fockenberg, T., Schreyer, W., 1997. Synthesis and chemistry of unusual excess-Si aluminous enstatite in the system MgO-Al2O3-SiO2 (MAS). Eur. J. Mineral. 9, 509–518.
Ford, W.E., Bradley, W.M., 1913. Pyroxmangite, a new member of the pyroxene group and its alteration product, skemmatite. Am. J. Sci. 212, 169–174.
Genna, A., Nehlig, P., Le Goff, E., Guerrot, C., Shanti, M., 2002. Proterozoic tectonism of the Arabian Shield. Precambrian Res. 117, 21–40.
Green, T.H., 1980. Island arc and continent-building magmatism: a review of petrogenetic models based on experimental petrology and geochemistry. Tectonophysics 63, 367–385.
Grey, I.E., Reid, A.F., 1975. The structure of pseudorutile and its role in the natural alteration of ilmenite. Am. Mineral. 60 (9–10), 898–906.
Hanson, G.N., 1978. The application of trace elements to the petrogenesis of igneous rocks of granitic composition. Earth Planet. Sci. Lett. 38, 26–43.
Harris, N.B., Pearce, J.A., Tindle, A.G., 1986. Geochemical characteristics of collision-zone magmatism. In: Coward, M.P., Ries, A.C. (Eds.), Collision Tectonics, 19. Journal of Geological Society, London, Special Publication, pp. 67–81.

Hawthorne, F.C., Oberti, R., Harlow, G.E., Maresch, W.V., Martin, R.F., Schumacher, J. C., Welch, M.D., 2012. IMA report, nomenclature of the amphibole supergroup. Am. Mineral. 97, 2031–2048.
Hereher, M.E., Abdullah, S.E., 2017. Lithologic mapping of Aja granitic batholiths, Ha'il, Saudi Arabia, using remote sensing. Arab. J. Geosci. 10, 313.
Jackson, N.J., Douch, C.J., 1986. Jabal Hamra REE-mineralized silexite, Hijaz region, Kingdom of Saudi Arabia. J. Afr. Earth Sci. 4, 269–274.
Jefferson, D.A., Pugh, N.J., Alario-Franco, M., Mallison, L.G., Millward, G.R., Thomas, J. M., 1980. The ultrastructure of pyroxenoid chain silicates. I. Variation of the chain configuration in rhodonite. Acta Crystallogr. Sect. A 36, 1058–1065.
Johnson, P.R., 2003. Post-amalgamation basins of the NE Arabian shield and implications for Neoproterozoic III tectonism in the northern East African orogen. Precambrian Res. 123, 321–338.
Johnson, P.R., Kattan, F.K., 2012. The geology of the Arabian Shield. A review of the geology of Precambrian rocks. In: Kingdom of Saudi Arabia. SGS, Special Publication, Riyadh.
Küster, D., 2009. Granitoid-hosted Ta mineralization in the Arabian–Nubian Shield: ore deposit types, tectono-metallogenetic setting, and petrogenetic framework. Ore Geol. Rev. 35, 68–86.
Liebau, F., 1959. Über die Kristallstruktur des Pyroxmangits (Mn, Fe, Ca, Mg) SiO3. Acta Crystallogr. 12 (3), 177–181.
Liégeois, J.P., Black, R., 1987. Alkaline magmatism subsequent to collision in the Pan-African belt of the Adrar des Iforas. In: Fitton, J.G., Upton, B.G.J. (Eds.), Alkaline Igneous Rocks, 30. Geological Society, Special Publication, pp. 381–401.
Liégeois, J.P., Navez, J., Black, R., Hertogen, J., 1998. Contrasting origin of post-collision high-K calc-alkaline and shoshonitic versus alkaline and peralkaline granitoids. The use of sliding normalization. Lithos 45, 1–28.
Lister, G.S., Davis, G.A., 1989. The origin of metamorphic core complexes and detachment faults formed during Tertiary continental extension in the northern Colorado River region, USA. J. Struct. Geol. 11 (1/2), 65–94.
Ma, C., Tschauner, O., Beckett, J.R., Liu, Y., Rossman, G.R., Zhuravlev, K., Prakapenka, V., Dera, P., Taylor, L.A., 2015. Tissintite, $(Ca,Na,\gamma)AlSi_2O_6$, a highly-defective, shock-induced, high-pressure clinopyroxene in the Tissint martian meteorite. Earth Planet. Sci. Lett. 422, 194–205.
Ma, C., Tschauner, O., Kong, M., Beckett, J.R., Greenberg, E., Prakapenka, V.B., Lee, Y., 2021. A high-pressure, clinopyroxene-structured polymorph of albite in highly shocked terrestrial and meteoritic rocks. Am. Mineral. https://doi.org/10.2138/am-2021-7925 in press.
Maresch, W.V., Mottana, A., 1976. The pyroxmangite-rhodonite transformation for the $MnSiO_3$ composition. Contrib. Mineral. Petrol. 55, 69–79.
McKay, G.A., 1989. Partitioning of rare earth elements between major silicate minerals and basaltic melts. In: Lipin, B.R., McKay, G.A. (Eds.), Geochemistry and Mineralogy of Rare Earth Elements, 21. Mineralogical Society of America, pp. 45–77.
Meert, J.G., 2003. A synopsis of events related to the assembly of eastern Gondwana. Tectonophysics 362, 1–40.
Michailidis, K., Sofianska, E., 2010. Spheroidal and radiating aggregates of Mn-pyroxenoids in the Olympias carbonate-hosted polymetallic sulphide ore deposit, E. Chalkidiki peninsula, N. Greece. Rev. Bulgarian Geol. Soc. 71 (1–3), 59–68.
Millsteed, P.W., Mernagh, T.P., Otieno-Alego, V., Creagh, D.C., 2005. Inclusions in transparent gem rhodonite from Broken Hill, New South Wales, Australia. Gems Gemol. 41 (3), 246–254.
Moghazi, A.M., Harbi, H.M., Ali, K.A., 2011. Geochemistry of the Late Neoproterozoic Hadb adh Dayheen ring complex, Central Arabian Shield: implications for the origin of rare-metal-bearing post-orogenic A-type granites. J. Asian Earth Sci. 42, 1324–1340.
Moghazi, A.K.M., Iaccheri, L.M., Bakhsh, R.A., Kotov, A.B., Ali, K.A., 2015. Sources of rare-metal-bearing A-type granites from Jabel Sayed complex, Northern Arabian Shield, Saudi Arabia. J. Asian Earth Sci. 107, 244–258.
Morimoto, N., Fabries, J., Ferguson, A.K., Ginzburg, I.V., Ross, M., Seifert, F.A., Zussman, J., Aoki, K., Gottardi, G., 1988. Nomenclature of pyroxenes. Mineral. Mag. 52, 535–550.
Nehlig, P., Genna, A., Asfirane, F., 2002. A review of the Pan-African evolution of the Arabian Shield. GeoArabia 7, 103–124.
Nelson, D.G., Featherstone, J.D., 1982. Preparation, analysis, and characterization of carbonated apatites. Calcif. Tissue Int. 34, S69–S81.
Ohashi, Y., Kato, A., Matsubara, S., 1975. Pyroxenoids: a variation in chemistry of natural rhodonite and pyroxmangite. In: In Carnegie Institution of Washington Year Book 75.
Patiño Douce, A.E., 1999. What do experiments tell us about the relative contributions of crust and mantle to the origin of granitic magmas? In: Castro, A., Fernandez, C., Vigneresse, J. (Eds.), Understanding Granites: Integrating New and Classical Techniques, 168. Geological Society, London, Special Publications, pp. 55–75.
Pearce, J.A., Harris, N.B.W., Tindle, A.G., 1984. Trace element discrimination diagrams for the tectonic interpretation of granitic rocks. J. Petrol. 25, 956–983.
Pinckney, L.R., Burnham, C.W., 1988. Effects of compositional variation on the crystal structures of pyroxmangite and rhodonite. Am. Mineral. 73, 798–808.
Qadhi Talal, M., 2007. Geochemical evolution of rare metal-bearing A-type granites from the Aja Batholith, Hail Terrain, Saudi Arabia. J. Geol. Soc. India 70 (5), 714–729.
Qin, L., Humayun, M., 2008. The Fe/Mn ratio in MORB and OIB determined by ICP-MS. Geochim. Cosmochim. Acta 72, 1660–1677.
Robinson, F.A., Foden, J.D., Collins, A.S., Payne, J.L., 2014. Arabian Shield magmatic cycles and their relationship with Gondwana assembly: insights from zircon U–Pb and Hf isotopes. Earth Planet. Sci. Lett. 408, 207–225.
Sami, M., Ntaflos, T., Mohamed, H.A., Farahat, E.S., Hauzenberger, C., Mahdy, N.M., Abdelfadil, K.M., Fathy, D., 2020. Origin and petrogenetic implications of spessartine garnet in highly fractionated granite from the central Eastern Desert of Egypt. Acta Geol. Sin. Engl. Ed. 94 (3), 763–776.
Sauerzapf, U., Lattard, D., Burchard, M., Engelmann, R., 2008. The titanomagnetite–ilmenite equilibrium: new experimental data and thermo-oxybarometric application to the crystallization of basic to intermediate rocks. J. Petrol. 49, 1161–1185.
Seddik, A.M., Darwish, M.H., Azer, M.K., Asimow, P.D., 2020. Assessment of magmatic versus post-magmatic processes in the Mueilha rare-metal granite, Eastern Desert of Egypt, Arabian-Nubian Shield. Lithos 105542.
Sisson, T.W., 1994. Hornblende-melt trace-element partitioning by ion microprobe. Chem. Geol. 117, 331–344.
Stern, R.J., 1994. Arc assembly and continental collision in the Neoproterozoic East African Orogen: implications for the consolidation of Gondwanaland. Annu. Rev. Earth Planet. Sci. 22, 319–351.
Stern, R.J., Johnson, P.R., 2010. Continental lithosphere of the Arabian Plate: a geologic, petrologic, and geophysical synthesis. Earth Sci. Rev. 101, 29–67.
Stoeser, D.B., 1986. Distribution and tectonic setting of plutonic rocks of the Arabian shield. J. Afr. Earth Sci. 4, 21–46.
Stoeser, D.B., Frost, C.D., 2006. Nd, Pb, Sr, and O isotopic characterization of Saudi Arabian Shield terranes. Chem. Geol. 226, 163–188.
Stuckless, J.S., Hedge, C.E., Wenner, D.B., Nkomo, I.T., 1984. Isotopic studies ofpostorogenic granites from the northeastern Arabian Shield, Kingdom of Saudi Arabia. In: Saudi Arabian Deputy Ministry for Mineral Resources Open-File Report USGS-04-42, p. 57, 40 pp. Also, 1985, U.S. Geological Survey Open-File Report 85-726.
Sun, S.S., McDonough, W.F., 1989. Chemical and isotopic systematics of oceanic basalts: implications for mantle composition and processes. Geol. Soc. Lond., Spec. Publ. 42, 313–345.
Sylvester, P.J., 1989. Post-collisional alkaline granites. J. Geol. 97 (3), 261–280.
Villa, I.M., Ruggieri, G., Puxeddu, M., 1997. Petrological and geochronological discrimination of two white mica generations in a granite cored from the Larderello-Travale geothermal field (Italy). Eur. J. Mineral. 9, 563–568.
Whalen, J.B., Currie, K.L., Chappell, B.W., 1987. A-type granites: geochemical characteristics, discrimination and petrogenesis. Contrib. Mineral. Petrol. 95 (4), 407–419.
Wood, B.J., Henderson, C.M.B., 1978. Compositions and unit-cell parameters of synthetic non-stoichiometric tschermakitic clinopyroxenes. Am. Mineral. 63 (1–2), 66–72.
Wu, F.-Y., Sun, D.-Y., Li, H., Jahn, B.-M., Wilde, S., 2002. A-type granites in northeastern China: age and geochemical constraints on their petrogenesis. Chem. Geol. 187, 143–173.